

RESEARCH ARTICLE

Repositioning of anti-dengue compounds against SARS-CoV-2 as viral polyprotein processing inhibitor

Leena H. Bajrai^{1,2}, Arwa A. Faizo^{1,3}, Areej A. Alkhaldy^{1,4}, Vivek Dhar Dwivedi^{5,6*}, Esam I. Azhar^{1,3*}

1 Special Infectious Agents Unit – BSL3, King Fahd Medical Research Center, King Abdulaziz University, Jeddah, Saudi Arabia, **2** Biochemistry Department, Faculty of Sciences, King Abdulaziz University, Jeddah, Saudi Arabia, **3** Department of Medical Laboratory Sciences, Faculty of Applied Medical Sciences, King Abdulaziz University, Jeddah, Saudi Arabia, **4** Clinical Nutrition Department, Faculty of Applied Medical Sciences, King Abdulaziz University, Jeddah, Saudi Arabia, **5** Center for Bioinformatics, Computational and Systems Biology, Pathfinder Research and Training Foundation, Greater Noida, India, **6** Bioinformatics Research Division, Quanta Calculus, Greater Noida, India

* vivek_bioinformatics@yahoo.com (VDD); eazhar@kau.edu.sa (EIA)



OPEN ACCESS

Citation: Bajrai LH, Faizo AA, Alkhaldy AA, Dwivedi VD, Azhar EI (2022) Repositioning of anti-dengue compounds against SARS-CoV-2 as viral polyprotein processing inhibitor. PLoS ONE 17(11): e0277328. <https://doi.org/10.1371/journal.pone.0277328>

Editor: Chandrabose Selvaraj, Alagappa University, INDIA

Received: June 14, 2022

Accepted: October 24, 2022

Published: November 16, 2022

Copyright: © 2022 Bajrai et al. This is an open access article distributed under the terms of the [Creative Commons Attribution License](#), which permits unrestricted use, distribution, and reproduction in any medium, provided the original author and source are credited.

Data Availability Statement: All relevant data are within the paper and its [Supporting information](#) files.

Funding: This project was funded by the Deanship of Scientific Research (DSR) at King Abdulaziz University, Jeddah, under grant number: GCV19-46-1441. The authors therefore acknowledge with thanks DSR for technical and financial support.

Competing interests: The authors have declared that no competing interests exist.

Abstract

A therapy for COVID-19 (Coronavirus Disease 19) caused by Severe Acute Respiratory Syndrome Coronavirus 2 (SARS-CoV-2) remains elusive due to the lack of an effective anti-viral therapeutic molecule. The SARS-CoV-2 main protease (M^{pro}), which plays a vital role in the viral life cycle, is one of the most studied and validated drug targets. In Several prior studies, numerous possible chemical entities were proposed as potential M^{pro} inhibitors; however, most failed at various stages of drug discovery. Repositioning of existing antiviral compounds accelerates the discovery and development of potent therapeutic molecules. Hence, this study examines the applicability of anti-dengue compounds against the substrate binding site of M^{pro} for disrupting its polyprotein processing mechanism. An *in-silico* structure-based virtual screening approach is applied to screen 330 experimentally validated anti-dengue compounds to determine their affinity to the substrate binding site of M^{pro} . This study identified the top five compounds (CHEMBL1940602, CHEMBL2036486, CHEMBL3628485, CHEMBL200972, CHEMBL2036488) that showed a high affinity to M^{pro} with a docking score > -10.0 kcal/mol. The best-docked pose of these compounds with M^{pro} was subjected to 100 ns molecular dynamic (MD) simulation followed by MM/GBSA binding energy. This showed the maximum stability and comparable ΔG binding energy against the reference compound (X77 inhibitor). Overall, we repurposed the reported anti-dengue compounds against SARS-CoV-2- M^{pro} to impede its polyprotein processing for inhibiting SARS-CoV-2 infection.

1. Introduction

Pharmaceutical research into the discovery and development of therapeutic compounds has expanded rapidly since the emergence of COVID-19 (a disease caused by SARS-CoV-2

infection) [1–3]. Target-based drug discovery has been investigated exponentially due to the release of experimental structures of essential structural and non-structural proteins of SARS-CoV-2 [4–6]. These proteins are used as drug targets in computational structure-based drug design, where virtual screening is performed against these targets to find the most potent antagonist compound [7–9]. The protease enzyme is involved in viral protein maturation by breaking down polypeptide sequences, which concludes the infection life cycle of the virus [10, 11], making the protease enzyme a promising therapeutic target [12, 13]. Main protease (M^{Pro})' functional role in SARS-CoV-2 growth established its potential clinical use in the drug discovery pipeline [14, 15]. In the case of other viruses, several therapeutic molecules have been developed to target their corresponding M^{Pro} structure. Several compounds, including nelfinavir, ritonavir, indinavir, atazanavir, saquinavir, lopinavir, amprenavir, darunavir, and tipranavir, are effective protease inhibitors in HIV [16]. Similarly, among hepatitis C virus compounds, sofosbuvir, voxilaprevir, glecaprevir, grazoprevir, paritaprevir, asunaprevir, ritonavir, telaprevir, and boceprevir were the FDA approved therapeutic molecules [17].

The M^{Pro} protein of SARS-CoV-2 is a cysteine protease that cleaves itself between the nsp4 and nsp6, followed by the cleavage of other polypeptide regions resulting in the maturation of viral proteins, which is required for virus replication [18–20]. M^{Pro} is a homodimer protein; each protomer contains three domains, viz. Domain-I from 8 to 101, Domain II from 102 to 184, and Domain III from 201 to 303 amino acid residues. Domains I and II contain antiparallel β -barrel structures and together, they form a cleft possessing a Cys-His catalytic dyad which serves as a substrate binding site similar to other coronavirus families. However, Domain III is a helical domain with 5 α -helices that form a globular structure and is connected to Domain II via a 15-residue long loop structure. [21–23]. The N-terminal finger (residues 1 to 7) located between domain II and domain III of each protomer forms a connecting link between the protomer forming the substrate binding site in a cleft which is located between domain I and domain II [24–28]. The monomeric SARS-CoV-2 M^{Pro} is functionally inactive for polyprotein processing and therefore the dimerization interface serving the substrate binding site is targeted to develop potential therapeutics in this study [29, 30]. Multiple crystal structures of SARS-CoV-2 M^{Pro} have been solved, which facilitated novel drug design and drug repurposing [31–47].

Structure-based virtual screening is widely used in drug discovery using the SARS-CoV-2 M^{Pro} protein crystal structure, and the ultra large chemical library was screened against the active site where the compound selection was guided by the crystal structure information and docking-based screening [48]. Ligand-based drug design (LBDD) was also used in several studies where pharmacophores were designed using known inhibitors and further screened in the ZINC library [49, 50]. A study illustrated computational tools and techniques to design peptidomimetic inhibitors against SARS-CoV-2 M^{Pro} [51]. The natural compound library was screened in several cases to identify the potential M^{Pro} inhibitor using molecular docking and MM/PBSA method [52]. The efficiency of current antiviral compounds against SARS-CoV-2 M^{Pro} was also evaluated using molecular docking and modelling as part of a drug repurposing effort [53].

Moreover, experimental findings of inhibitors were also validated using molecular dynamics simulation to understand the molecular level interaction between proteins and small molecules [54]. Among natural compounds or their derivatives, flavonoid compounds were extensively used in various computation screening studies against M^{Pro} [55–62]. Many antiviral compounds were evaluated computationally against SARS CoV-2 M^{Pro} to detect their repurposing effect. However, experimentally validated anti-dengue compounds were not comprehensively explored against SARS-CoV-2 M^{Pro} . In recent work, Murtuja et al. demonstrated the development of DENV inhibitors with a targeted comparison of a protease between DENV and SARS-CoV-2 [62].

In this study, a structure-based screening was performed against the SARS-CoV-2 M^{pro} using the known DENV inhibitors. These are experimentally validated DENV inhibitors (anti-viral compounds). Therefore with high hopes of finding promising antiviral therapeutic molecules against another viral protein, i.e., SARS-CoV-2 M^{pro}, they were tested by employing docking and molecular dynamics simulation techniques. In the first phase, the binding of these compounds with M^{pro} at its active site was determined using multilevel docking with standard and additional precision algorithms of the Glide tool. Top 5 compounds selected based on docking scores were: (1) N-benzoyl-L-norleucyl-L-lysyl-L-arginyl-2-phenyl-L-glycinal, (CHEMBL1940602) (2) (E)-7-[8-[(E)-6-carboxy-1-phenylhex-1-en-3-yl]-5,7-dihydroxy-4-oxo-2-phenyl-2,3-dihydrochromen-6-yl]-7-phenylhept-5-enoic acid (CHEMBL2036486), (3) [2-[(2S,3R,4S,5S,6R)-3-benzoyloxy-6-(benzoyloxymethyl)-4,5-dihydroxyoxan-2-yl]oxy-5-hydroxyphenyl]methyl (2R,3S,4S)-1,2,3,4-tetrahydroxy-5-oxocyclohexane-1-carboxylate (Flacourtoside D) (CHEMBL3628485), (4) [2-[(2S,3R,4S,5S,6R)-3-benzoyloxy-6-(benzoyloxymethyl)-4,5-dihydroxyoxan-2-yl]oxy-5-hydroxyphenyl]methyl (1R,2R,6R)-6-benzoyloxy-1,2-dihydroxy-5-oxocyclohex-3-ene-1-carboxylate (Flacourtoside F) (CHEMBL200972), and (5) (2S)-6-amino-N-[(1S)-2-amino-2-oxo-1-phenylethyl]-2-[(2S)-3-[4-(diaminomethylideneamino)phenyl]-2-(3 phenylpropanoylamino) propanoyl] amino]hexanamide (CHEMBL2036488). In addition, this study used a known M^{pro} inhibitor to compare the binding of screened compounds against the protein target. The control compound (X77 inhibitor: N-(4-tert-butylphenyl)-N-[(1R)-2-(cyclohexylamino)-2-oxo-1-(pyridin-3-yl) ethyl]-1H-imidazole-4-carboxamide) was sourced from the crystal structure of protein where it was co-crystallized with SARS-CoV-2 M^{pro} as a potential non-covalent inhibitor. MM/GBSA binding energy of all these top 5 screened compounds and the control (X77) was calculated over the complete trajectory of 100 ns MD simulation time. Overall, this study demonstrates the potential of five known DENV inhibitors to suppress SARS-CoV-2-M^{pro} activity.

2. Materials and methods

This study involved comprehensive molecular docking and molecular dynamic simulation in screening anti-DENV compounds against SARS-CoV-2 M^{pro}.

2.1 Structures collection

The protein structure of SARS-CoV-2 M^{pro} was sourced from the protein data bank (PDB) [63] with PDB ID: 6W63 (<https://www.rcsb.org/structure/6W63>). This structure contains the SARS-CoV-2 main protease solved using the X-ray diffraction technique at 2.10 Å resolution. It consists of single chain ‘A’ with 306 amino acids with a broad spectrum non-covalent inhibitor N-(4-tert-butylphenyl)-N-[(1R)-2-(cyclohexylamino)-2-oxo-1-(pyridine-3-yl)ethyl]-1H-imidazole-4-carboxamide labelled as X77 in the PDB entry. As illustrated in Fig 1, this co-crystallized inhibitor is placed at the interface of domains I and II of the protein.

The compound library was prepared from DenvInD databases (<https://webs.iiitd.edu.in/raghava/denvind/>) that store the active inhibitors against the dengue virus [64]. The study started with 330 compounds collected from the DenvInD database that were further prepared using the default parameters of the LigPrep panel in the Schrödinger suite [65]. During the ligand preparation, pH was set at 7.0 ± 2.0, and the OPLS-2005 force field was used to assign charge and radius to each ligand atom.

2.2 Docking preparation

This study primarily depends on the structure-based virtual screening (SBVS), where the receptor structure (PDB ID: 6W63) was prepared for docking using the protein preparation

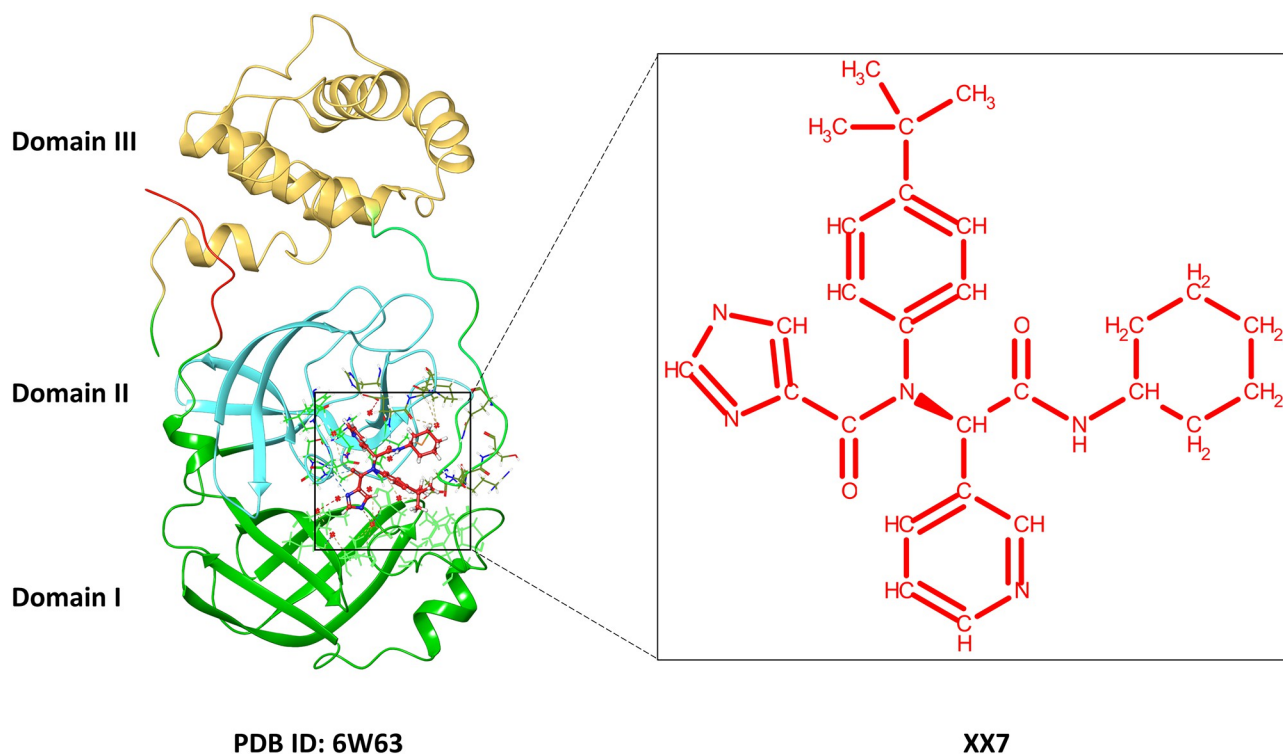


Fig 1. Crystal structure of M^{pro} (PDB ID: 6W63) representing Domain I, II and III with the co-crystallized ligand (PDB code: X77).

<https://doi.org/10.1371/journal.pone.0277328.g001>

wizard of the Schrödinger suite [66]. Here, the missing atoms were added to the protein structure with the assignment of partial and formal charges to the molecule. Co-crystallized water molecules were removed to allow free docking of new compounds to the protein's active site.

The information from a native (X77 inhibitor) ligand bound with the structure was used to create a docking grid that covered all essential residues grid centre at -20.46 (X), 18.11 (Y), -26.9 Å (Z) region. The inner-box size 10 X10 X 10 Å and outer-box size 25.094 X 25.094 X 25.094 were set along X, Y, and Z axes using the grid generation tool of the Schrödinger suite to allow the ligand docking with the SARS-CoV-2 M^{pro} active site with all possible confirmations. His41 and Cys145 constitute the catalytic duo of SARS-CoV-2 M^{pro}, and the grid box was constructed around these two catalytic residues. In addition, residues that demonstrated active contact with X77 inhibitor in its PDB structure were considered during grid generation. Glu166, His163, and Gly143 form direct H-bonds with X77. Other polar and nonpolar residues close to the ligand also assisted in making the grid. These included Gln189, Asp187, His164, Thr25, Thr26, Asn142, Met165, Phe140, Ser144, and Leu141 residues.

2.3 Structure-based virtual screening workflow

In the first phase, compounds were screened using high throughput virtual screening of the Schrödinger suite. Later the filtered compounds were docked in the defined grid using the Glide standard precision (SP) and extra precision (XP) modules of the Schrödinger suite [67–70]. Reference compound X77 was removed from the PDB structure and redocked at the defined grid site. All docked poses were analysed for intermolecular interactions using the default settings of Maestro v12.9, and 3D and 2D interaction diagrams were generated using the free academic edition of Maestro v12.9 [71].

2.4 Molecular dynamic simulation

The top poses of five compounds and the reference compound were simulated further using the Desmond-maestro 2020–4 academic package [72, 73]. Every docked pose was placed in a 10 Å × 10 Å × 10 Å orthorhombic box and an explicit solvent molecule (TIP4P: transferable intermolecular potential 4 point) was added with 0.15 M salt concentration to bring the system to a physiological state. Later, the system was neutralized by adding the appropriate number of Na⁺ and Cl⁻ ions. In the first phase of simulation, the complete system was minimized under the default parameters of the simulation. Post minimization, a 100 ns simulation was performed under the OPLS-2005 force field at 300 K temperature. The simulation trajectory was further analysed using the root mean square deviation (RMSD) of Cα atoms of protein using Eq (1).

$$RMSD_x = \sqrt{\frac{1}{N} \sum_{i=1}^N (r'_i(t_x) - r_i(t_{ref}))^2} \quad (1)$$

N : the number of atoms selected; t_{ref} : reference time at zero interval; r_i : position of the atoms under evaluation in frame x; r'_i : position of the atoms in the reference frame; t_x : time frame for RMSD calculation.

In addition, each protein residue's fluctuation was calculated using root mean square fluctuation (RMSF) as per Eq 2.

$$RMSF_i = \sqrt{\frac{1}{T} \sum_{t=1}^T (r'_i(t) - r_i(t_{ref}))^2} \quad (2)$$

T : simulation interval; t_{ref} : reference time; r_i : position of the atoms under evaluation in frame x; r'_i : position of the atoms in the reference frame.

2.5 Binding free energy calculation

The binding free energy for the complete trajectory (100 ns) was calculated using the MM/GBSA model of the Prime Schrödinger suite (Script-thermal_mmgbasa.py) [74–76]. This tool calculates the binding energy of protein and ligand by deploying molecular mechanics force field calculation and generalized born solvent model [77]. The molecular mechanics (MM) component represents the internal energy of the system consisting of bonded (bond energy, angle energy, dihedral energy) and non-bonded (van der Waal, electrostatic) interactions between protein and ligand. The change in bonded interaction in the free and bound state of protein and ligand is the same, implying $\Delta G_{\text{Bonded/Internal Energy}} \approx 0$. Thus, only non-bonded interaction contributed to ΔG . Moreover, the generalized born solvent model also consists of polar solvation energy (GB) and non-polar solvation energy (SA). Details of the binding free energy calculation are shown in Eq (3).

$$\Delta G_{\text{Bind}} = G_{\text{Complex(minimized)}} - (G_{\text{Receptor (minimized)}} - G_{\text{Ligand (minimized)}}) \quad (3)$$

$$\Delta G_{\text{Bind}} = \Delta H - T\Delta S \approx \Delta E_{\text{gas}} + \Delta G_{\text{sol}} - T\Delta S \quad (3.1)$$

$$\Delta E_{\text{gas}} = \Delta E_{\text{int}} + \Delta E_{\text{ele}} + \Delta E_{\text{vdw}} \quad (3.2)$$

$$\Delta G_{\text{sol}} = \Delta G_{\text{GB}} + \Delta G_{\text{surf}} \quad (3.3)$$

ΔG_{Bind} : Change in Binding free energy.

$G_{\text{Complex(minimized)}}$: Free energy of the complex
 $G_{\text{Receptor (minimized)}}$: Free energy for the receptor
 $G_{\text{Ligand (minimized)}}$: Free energy for the ligand
 ΔH : Change in enthalpy
 ΔS : Change in entropy (neglected in this equation ≈ 0)
 ΔE_{gas} : Change in gas phase interaction energy
 ΔE_{int} : Change in internal energy (no change as the same receptor and ligand is considered for the trajectory ≈ 0)
 ΔG_{sol} : Change in solvation energy
 ΔG_{GB} : Polar Solvation energy
 ΔG_{surf} : Non-polar solvation energy.

3. Results and discussions

3.1 Native ligand interactions

The native ligand (X77) co-crystallized with the M^{Pro} was initially analysed for the native contacts as shown in Fig 2. It has been observed that catalytic dyads Cys145 and His41 were placed

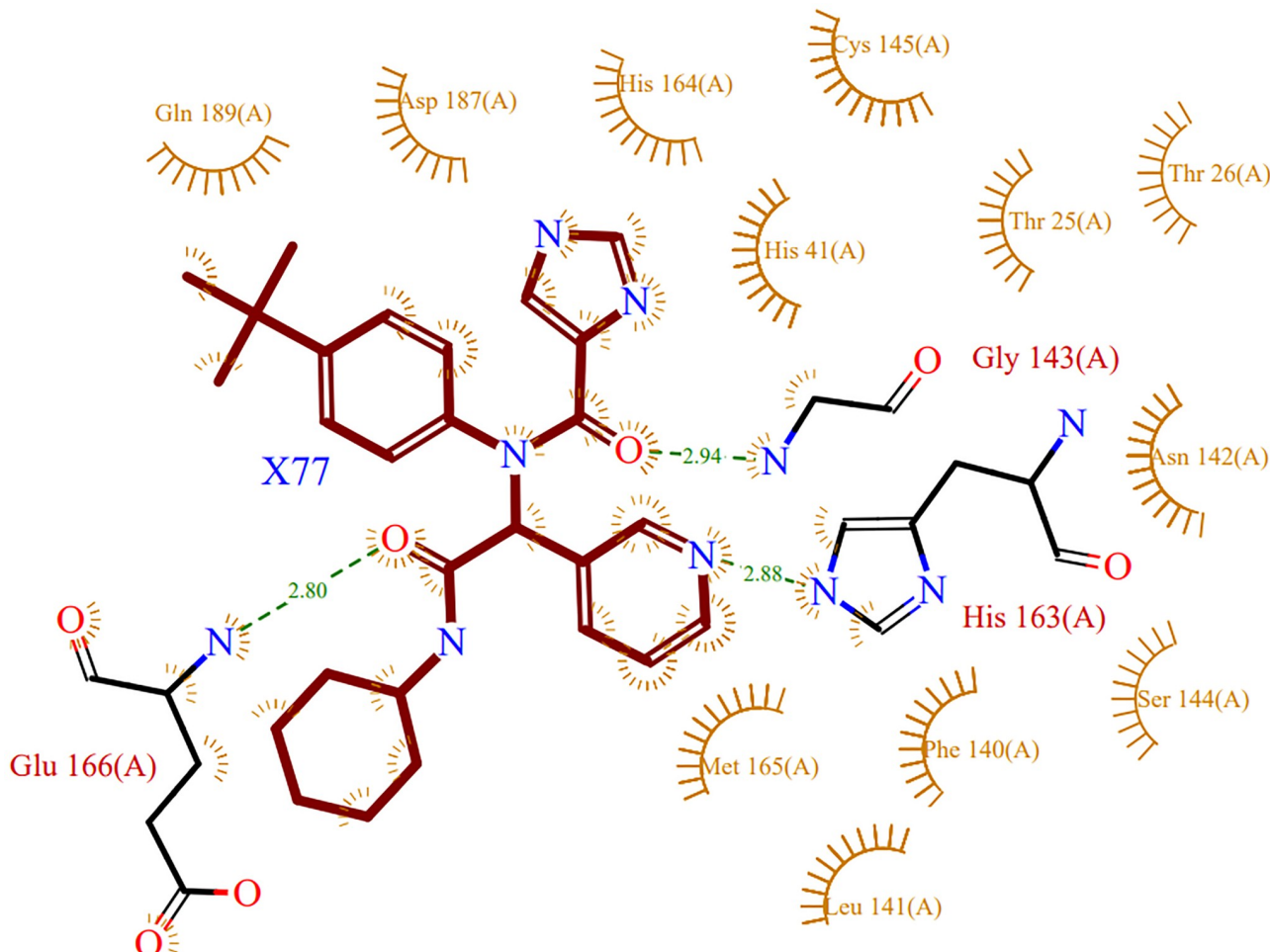


Fig 2. Native ligand (X77)-protein (PDB structure 6W63) 2D interactions plot: Representation of intermolecular interaction between native ligand and the active site amino acid residue of the target protein.

<https://doi.org/10.1371/journal.pone.0277328.g002>

in the proximity of the ligand, which indicates the possible inhibitory properties of the ligand. Gly143, His163, and Glu166 formed hydrogen bonds with the ligand at 2.94Å, 2.88Å and 2.80Å hydrogen bond donor-acceptor distances.

3.2 Re-docking of native ligand

Native ligand X77 was removed from the PDB structure and redocked at the designated grid (description mentioned in the Methods section). The docking was performed using the Glide Schrödinger suite. This validated the docking protocol and used the native ligand as a control for further study. The best pose of the docked complex was studied to find the similarity between the native structure (PDB ID: 6W63) and the docked pose. In the native complex, it showed a total of 3 hydrogen bonds with Glu166, His163, and Gly143 each (Fig 2). However, in the best docked complex, Glu166 was retained while an additional Asn142 hydrogen bond was formed with the carboxyl oxygen of the ligand, which was initially bonded with Gly143 in its native form. His41, one of the catalytic dyad residues of SARS-CoV-2 M^{pro}, is involved in a π-π stacking interaction with the benzene ring of the ligand. These observations set the docked pose of the native ligand to be used as a control.

3.3 Virtual screening

This study used 330 anti-dengue compounds sourced from the DenvInD database. A list of these compounds is shown in S1 Table in [S1 File](#). All these compounds have antiviral properties and thus could be potential compounds for screening against the SARS-CoV-2 M^{pro}. These molecules were prepared in Ligprep to assign partial charge, radius, and van der Waal parameters. Each compound was used in multiple conformations to cover the possible relevant geometrical chemical space, and a total of 524 conformations were generated. These 524 conformers of 330 compounds that were initially screened using the HTVS (high-throughput virtual screening) protocol with 25% selection criteria. The result was 131 compounds for the next phase. In the next phase, Glide's standard precision (SP) protocol was applied for the docking, and the top 25% of compounds were selected. It resulted in 34 compounds being selected for the next phase of docking using the extra precision (XP) protocol of Glide. Here, XP also used a 25% selection filter based on the binding score calculated in Glide XP. This resulted in 7 compounds with the maximum possibility of interacting with SARS-CoV-2 M^{pro} at its binding site. However, three of the seven compounds were the same with different conformations, so only the one with the highest binding score was used, while the other two were eliminated. This made the final bin with the top 5 unique compounds for further study. Fig 3 shows the binding score of selected compounds at each screening protocol. Fig 3(a) shows the 131 compounds selected after HTVS; none of the compounds had a binding score greater than -6.5 kcal/mol. The best binding score -10.25 kcal/mol was shown by (+)-chartaceone D (Pubchem ID: 56834070), a flavonoid derivative.

Similarly, SP results is shown in Fig 3(b); here, 31 compounds were selected, and all showed binding energy better than -9.0 kcal/mol. In SP screening, the best binding score of -10.94 kcal/mol was shown by the tetrapeptide molecule H-Trp-Tyr-Cys-Trp-NH₂ (Pubchem ID 118717692). Moreover, Fig 3(c) shows the last 7 compounds screened after XP screening, where all the compounds had a binding score better than -10.0 kcal/mol. Here again, (+)-chartaceone D (Pubchem ID: 56834070) showed the best binding score of -10.61 kcal/mol. However, H-Trp-Tyr-Cys-Trp-NH₂ (Pubchem ID 118717692) showed the best binding score in Glide SP was eliminated after Glide XP screening.

As discussed, five unique compounds were selected after performing all three screening protocols, as shown in Fig 4 with their corresponding binding scores. These compounds are:

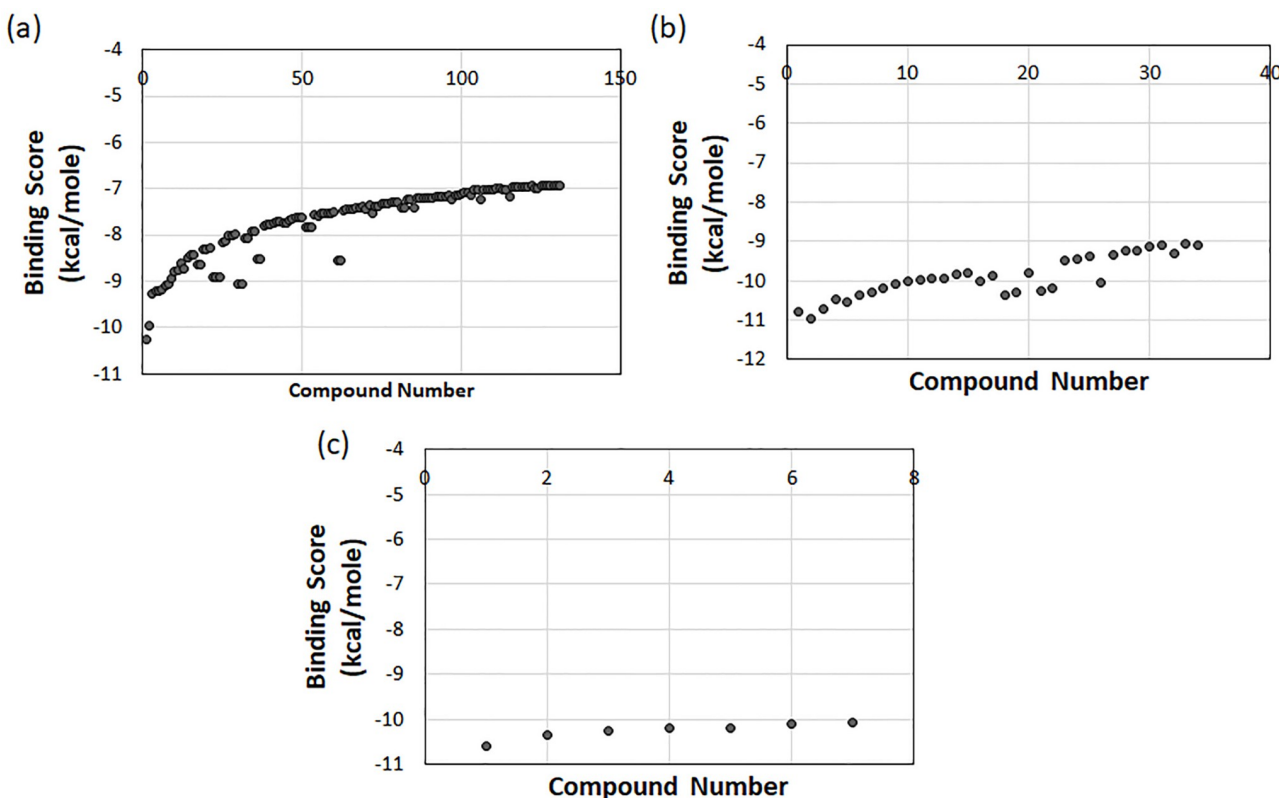


Fig 3. Binding scores of compounds were obtained via three different accuracy levels applied during the structure-based virtual screening process.
 (a) HTVS, (2) Glide SP, and (c) Glide XP.

<https://doi.org/10.1371/journal.pone.0277328.g003>

1. Pubchem ID 56834070: (E)-7-[8-[(E)-6-carboxy-1-phenylhex-1-en-3-yl]-5,7-dihydroxy-4-oxo-2-phenyl-2,3-dihydrochromen-6-yl]-7-phenylhept-5-enoic acid (+/-Chartaceone D)—labelled as CHEMBL1940602
2. Pubchem ID 57409246: [2-[(2S,3R,4S,5S,6R)-3-benzoyloxy-6-(benzoyloxymethyl)-4,5-dihydroxyoxan-2-yl]oxy-5-hydroxyphenyl]methyl (2R,3S,4S)-1,2,3,4-tetrahydroxy-5-oxocyclohexane-1-carboxylate (Flacourtoside D)—labelled as CHEMBL2036486
3. Pubchem ID 122193488: (2S)-6-amino-N-[(1S)-2-amino-2-oxo-1-phenylethyl]-2-[[[(2S)-3-[4-(diaminomethylideneamino)phenyl]-2-(3 phenylpropanoylamino) propanoyl] amino] hexanamide (deamino-Phe-Phe(4-guanidino)-Lys-Phg-NH2)—labelled as CHEMBL3628485
4. Pubchem ID 11974638: N-[(2S)-1-[[[(2S)-6-amino-1-[[[(2S)-5-(diaminomethylideneamino)-1-oxo-1-[(1S)-2-oxo-1-phenylethyl]amino]pentan-2-yl] amino]-1-oxohexan-2-yl]benzamide (Bz-Nle-Lys-Arg-Phg-al)—labelled as CHEMBL200972
5. Pubchem ID 57409350: [2-[(2S,3R,4S,5S,6R)-3-benzoyloxy-6-(benzoyloxymethyl)-4,5-dihydroxyoxan-2-yl]oxy-5-hydroxyphenyl]methyl (1R,2R,6R)-6-benzoyloxy-1,2-dihydroxy-5-oxocyclohex-3-ene-1-carboxylate (Flacourtoside F)—labelled as CHEMBL2036488

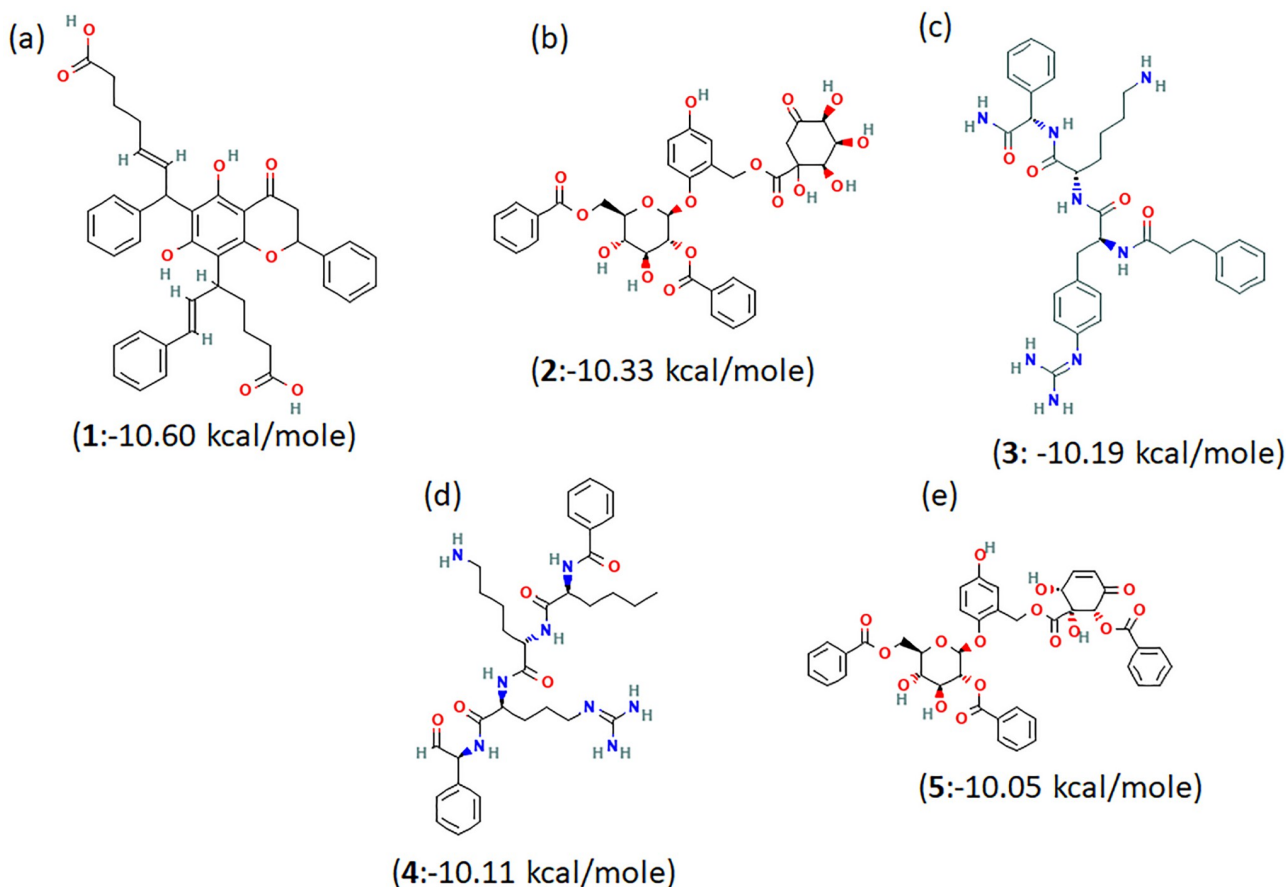


Fig 4. 2D chemical structures of top 5 compounds obtained via HTVS, SP and XP screening with their binding score. (a) CHEMBL1940602 (b) CHEMBL2036486 (c) CHEMBL3628485 (d) CHEMBL200972 and (e) CHEMBL2036488.

<https://doi.org/10.1371/journal.pone.0277328.g004>

3.4 ADME and toxicity analysis

The proposed molecules as therapeutics must be biologically active with minimum toxicity. Therefore, the selected compounds were studied for their pharmacokinetic features such as absorption, distribution, metabolism, excretion (ADME) and toxicity. Most drugs fail due to their least biological availability and higher toxicity at the clinical trial stages; therefore, assessing those parameters at the early stage of drug discovery is mandatory. The selected antiviral compounds were the non-inhibitors of cytochromes (CYP1A2, CYP2C19, CYP2C9, CYP2D6, and CYP3A4) which play an essential role in the metabolism of drugs and xenobiotics. All selected compounds were found to lack blood-brain barrier (BBB) features and lower gastrointestinal (GI) absorption, marked as an essential feature of drug molecules. The selected compounds were shown violations to the rules such as Lipinski, Ghose, Veber, Egan, and Mungan, which are considered an important rule of thumb to evaluate drug likeliness. However, these rules are not required to be followed strictly as several drugs in the past have violated these rules but still got FDA approval [78]. Among all five selected compounds, only CHEMBL1940602 showed an acceptable bioavailability score (0.56). Notably, All five compounds were found to be non-mutagenic as well as non-carcinogenic. Other pharmacological and drug-likeness features are also enlisted in S2 and S3 Tables [S1 File](#). Overall, the selected compounds obeyed the important ADMET parameters and can be considered for further studies.

3.5 Docked pose interaction

Screened molecules were further analysed for their interactions with SARS-CoV-2 M^{PRO} protein through its binding site residues, as shown in [Table 1](#) and [Fig 5](#). Compound 1 ([Fig 5\(a\)](#) and [5\(b\)](#)) has formed hydrogen bonds with Gly143 and Asn142. Both these residues form hydrogen bonds in the control compound (X77), Gly143 in the crystal structure and Asn142 in the best-docked pose of X77. CHEMBL2036486 ([Fig 5\(c\)](#) and [5\(d\)](#)) has the possibility of forming four hydrogen bonds with Gln189, His163, Glu166, and Asn142. It also contains two similar H-bond interactions shown with the control compound (X77); these are Glu166 (native form) and Asn142 (docked pose).

In CHEMBL3628485 ([Fig 5\(e\)](#) and [5\(f\)](#)), Glu166 showed the potential to form 6 H-bonds on its own, while Asn142, Thr190, and Gln192 each have the potential to form one H-bond. In terms of polar interaction, it was most likely that CHEMBL3628485 ([Fig 5\(g\)](#) and [5\(h\)](#)) would interact strongly with M^{PRO}. CHEMBL200972 also showed similar characteristics as CHEMBL3628485 and Glu166 showed the possibility to interact at five sites of the ligand with H-bonds. However, Phe140, Asn142, Pro168, and Gln189 were additional residues that formed 1 H-bond each with CHEMBL200972. Similar to CHEMBL1940602, CHEMBL2036486, and CHEMBL3628485, two residues (Glu166 and Asn142) had overlapping H-bond formation with control in their crystal and docked poses, respectively. CHEMBL2036488 ([Fig 5\(i\)](#) and [5\(j\)](#)) had a total of 6 H-bonds and 1 Π - Π stacking interaction. The stacking interaction formed by His41 (catalytic dyad residue) with the benzene ring of CHEMBL2036488 was also found in the best pose of the control compound ([Fig 5\(k\)](#) and [5\(l\)](#)). The control compound has H-bond interactions with Glu166 and Gly143 (Figs 2, [5\(k\)](#) and [5\(l\)](#)), which were also found in CHEMBL2036488. Another catalytic dyad residue (Cys145) also formed an H-bond with CHEMBL2036488. Additionally, Gln189 formed an H-bond similar to CHEMBL3628485.

3.6 Molecular dynamic (MD) simulation

Molecular dynamic simulation is an essential computational technique to establish the dynamic stability of protein-ligand interactions of docked complexes with respect to time. Best

Table 1. Intermolecular interactions noted for the screened compounds with the SARS-CoV-2 M^{PRO} within 4 Å around the docked ligand in the respective binding pockets.

Compounds	H-bond	Hydrophobic	Polar	π - π / $^*\pi$ - cation	Salt bridge	Positive	Negative
CHEMBL1940602	Asn ¹⁴² , ,Gly ¹⁴³ ,	Ley ²⁷ , Cys ⁴⁴ , Met ⁴⁹ , Phe ¹⁴⁰ , Leu ¹⁴¹ , Cys ¹⁴⁵ , Met ¹⁶⁵ , Leu ¹⁶⁷ , Pro ¹⁶⁸ .	Thr ²⁵ , Thr ²⁶ , His ⁴¹ , Thr ⁴⁵ , Ser ⁴⁶ , Asn ¹⁴² , Ser ¹⁴⁴ , His ¹⁶³ , His ¹⁶⁴ , His ¹⁷² , Gln ¹⁸⁹ , Thr ¹⁹⁰ , Gln ¹⁹² ,	--	--	Arg ¹⁸⁸	Glu ¹⁶⁶ , Asp ¹⁸⁷
CHEMBL2036486	Asn ¹⁴² , His ¹⁶³ , Glu ¹⁶⁶ , Gln ¹⁸⁹	Cys ⁴⁴ , Met ⁴⁹ , Phe ¹⁴⁰ , Leu ¹⁴¹ , Cys ¹⁴⁵ , Met ¹⁶⁵ , Leu ¹⁶⁷ , Pro ¹⁶⁸	Thr ²⁴ , Thr ²⁵ , His ⁴¹ , Thr ⁴⁵ , Ser ⁴⁶ , Asn ¹⁴² , Ser ¹⁴⁴ , His ¹⁶³ , His ¹⁶⁴ , His ¹⁷² , Gln ¹⁸⁹ , Thr ¹⁹⁰	--	--	Arg ¹⁸⁸	Glu ¹⁶⁶
CHEMBL3628485	Asn ¹⁴² , Glu ¹⁶⁶ , Leu ¹⁶⁷ , Thr ¹⁹⁰ , Gln ¹⁹²	Val ⁴² , Cys ⁴⁴ , Met ⁴⁹ , Phe ¹⁴⁰ , Leu ¹⁴¹ , Cys ¹⁴⁵ , Met ¹⁶⁵ , Leu ¹⁶⁷ , Pro ¹⁶⁸ , Val ¹⁸⁶	Thr ²⁵ , His ⁴¹ , Thr ⁴⁵ , Ser ⁴⁶ , Asn ¹⁴² , Ser ¹⁴⁴ , His ¹⁶³ , His ¹⁶⁴ , His ¹⁷² , Gln ¹⁸⁹ , Thr ¹⁹⁰ , Gln ¹⁹²	--	Glu ¹⁶⁶	Arg ¹⁸⁸	Glu ¹⁶⁶ , Asp ¹⁸⁷
CHEMBL200972	Phe ¹⁴⁰ , Asn ¹⁴² , Glu ¹⁶⁶ , Pro ¹⁶⁸ , Gln ¹⁸⁹	Ley ²⁷ , Met ⁴⁹ , Tyr ⁵⁴ , Phe ¹⁴⁰ , Leu ¹⁴¹ , Cys ¹⁴⁵ , Met ¹⁶⁵ , Leu ¹⁶⁷ , Pro ¹⁶⁸	Thr ²⁵ , Thr ²⁶ , His ⁴¹ , Asn ¹⁴² , Ser ¹⁴⁴ , His ¹⁶³ , His ¹⁶⁴ , His ¹⁷² , Gln ¹⁸⁹ , Thr ¹⁹⁰ , Gln ¹⁹² ,	--	Glu ¹⁶⁶	Arg ¹⁸⁸	Glu ¹⁶⁶ , Asp ¹⁸⁷
CHEMBL2036488	Gly ¹⁴³ , Cys ¹⁴⁵ , His ¹⁹³ , Glu ¹⁶⁶ , Gln ¹⁸⁹	Ley ²⁷ , Met ⁴⁹ , Phe ¹⁴⁰ , Leu ¹⁴¹ , Cys ¹⁴⁵ , Met ¹⁶⁵ , Leu ¹⁶⁷ , Pro ¹⁶⁸ , Ala ¹⁹¹	Thr ²⁴ , Thr ²⁵ , Thr ²⁶ , His ⁴¹ , Asn ¹⁴² , Ser ¹⁴⁴ , His ¹⁶³ , His ¹⁶⁴ , His ¹⁷² , Gln ¹⁸⁹ , Thr ¹⁹⁰ , Gln ¹⁹² ,	His ⁴¹	--	Arg ¹⁸⁸	Glu ¹⁶⁶ , Asp ¹⁸⁷
X77 (Control)	Asn ¹⁴² , His ¹⁶³ , Glu ¹⁶⁶	Ley ²⁷ , Val ⁴² , Cys ⁴⁴ , Met ⁴⁹ , Pro ⁵² , Thr ⁵⁴ , Phe ¹⁴⁰ , Leu ¹⁴¹ , Cys ¹⁴⁵ , Met ¹⁶⁵ ,	Thr ²⁵ , Thr ²⁶ , His ⁴¹ , Asn ¹⁴² , Ser ¹⁴⁴ , His ¹⁶⁶ , His ¹⁶⁴ , His ¹⁷² , Gln ¹⁸⁹	His ⁴¹	--	Arg ¹⁸⁸	Glu ¹⁶⁶ , Asp ¹⁸⁷

<https://doi.org/10.1371/journal.pone.0277328.t001>

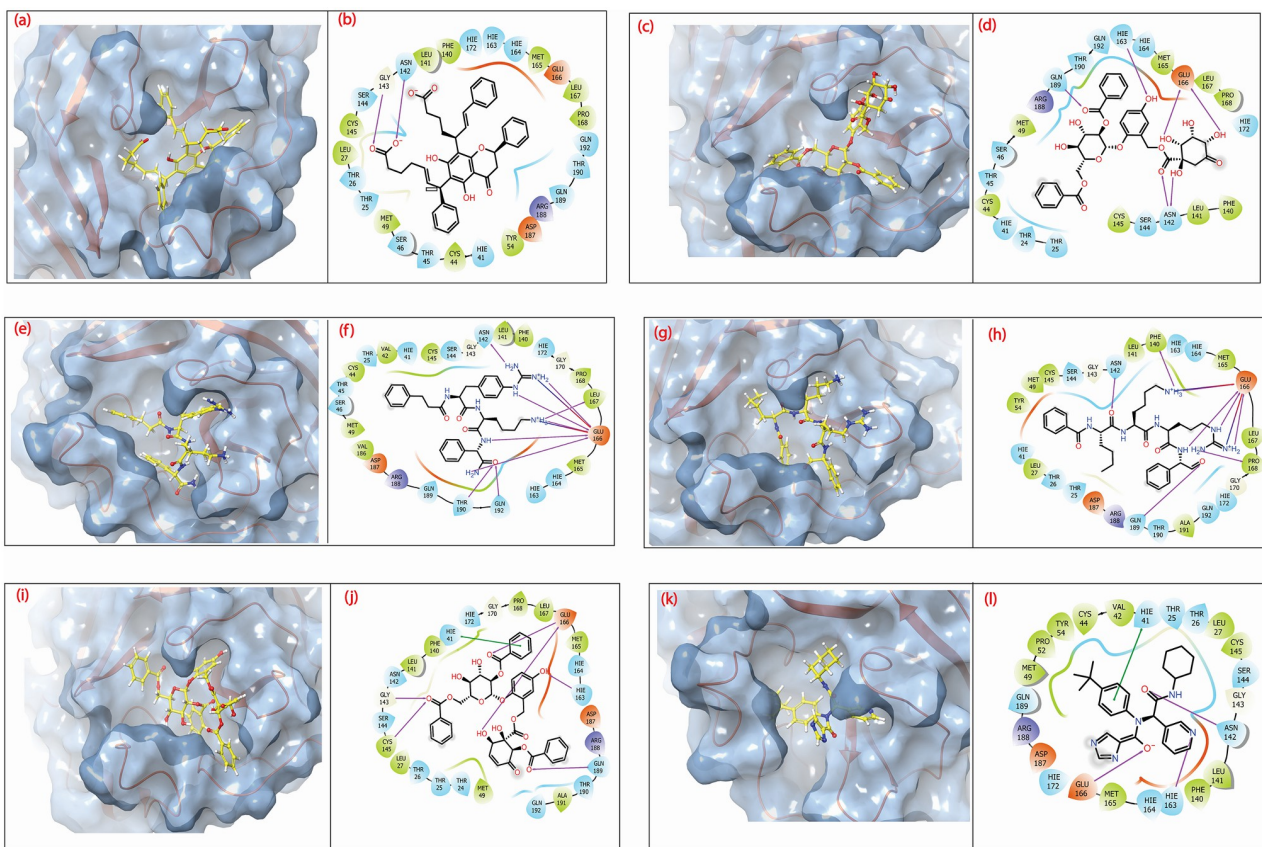


Fig 5. 3D and 2D interaction profiles for SARS-CoV-2 M^{Pro}- compounds (a-b) M^{Pro}-CHEMBL1940602 (c-d) M^{Pro}-CHEMBL2036486 (e-f) M^{Pro}-CHEMBL3628485 (g-h) M^{Pro}-CHEMBL200972 (i-j) M^{Pro}-CHEMBL2036488, and (k-l) M^{Pro}-X77 (control).

<https://doi.org/10.1371/journal.pone.0277328.g005>

docked poses of all screened and control compounds were used for 100 ns explicit MD simulation at 300 K temperature and 1 bar pressure. Later, the MD was also performed at 310 K (Human body temperature), and the results are given in [S2 File](#). MD trajectory of 100 ns was generated for all the selected complexes. Dynamic stability is shown in [Fig 6](#) and [S3 Fig](#) in [S1 File](#), where the initial pose (first frame of simulation) and final pose (last frame of simulation) are depicted. CHEMBL1940602, CHEMBL2036486, and CHEMBL200972 showed higher conformational consistency at the binding site, whereas CHEMBL3628485 and CHEMBL2036488 showed considerable translation and rotational movement to attain a more thermodynamically stable state. The control compound ([Fig 6\(f\)](#)) demonstrated the higher stability with the least amount of translation and rotation movement.

3.5.1 Root Mean Square Deviation (RMSD). RMSD over the trajectory measures the deviation of the system with respect to the first frame (original) state. Here, RMSD was computed over the whole trajectory for both protein and ligand separately to measure the equilibration stage of the protein-ligand complex. The conformational variance of less than 3 Å is deemed acceptable. If there is a minimum deviation, then the lines in the RMSD plot are parallel to the X-axis. [Fig 7](#) shows the RMSD of all screened and control compounds over the 100 ns trajectory. Protein RMSD in all cases was under 3 Å, and thus it did not show any significant deviation. Control shows the minimum deviation for protein and ligand <2 Å. Here, both Ligand^{RMSD} and Protein^{RMSD} were stable from the beginning of the simulation and maintained the same pattern until the completion of the experiment. Observing that both lines

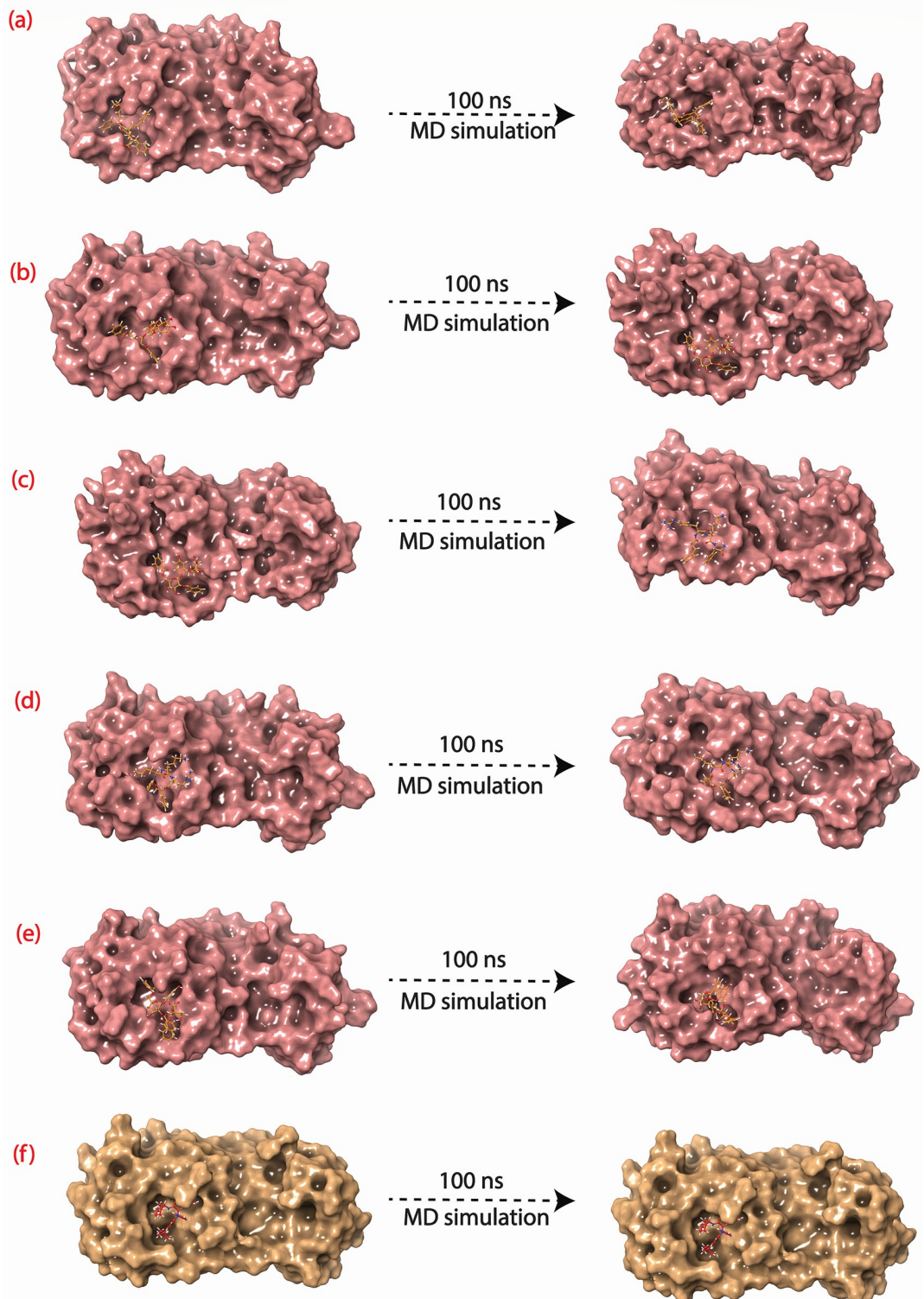


Fig 6. Dynamic flexibility depiction using first and last pose obtained from MD simulation for (a) M^{pro}-CHEMBL1940602 (b) M^{pro}-CHEMBL2036486 (c) M^{pro}-CHEMBL3628485 (d) M^{pro}-CHEMBL200972 (e) M^{pro}-CHEMBL2036488, and (f) M^{pro}-X77 (control).

<https://doi.org/10.1371/journal.pone.0277328.g006>

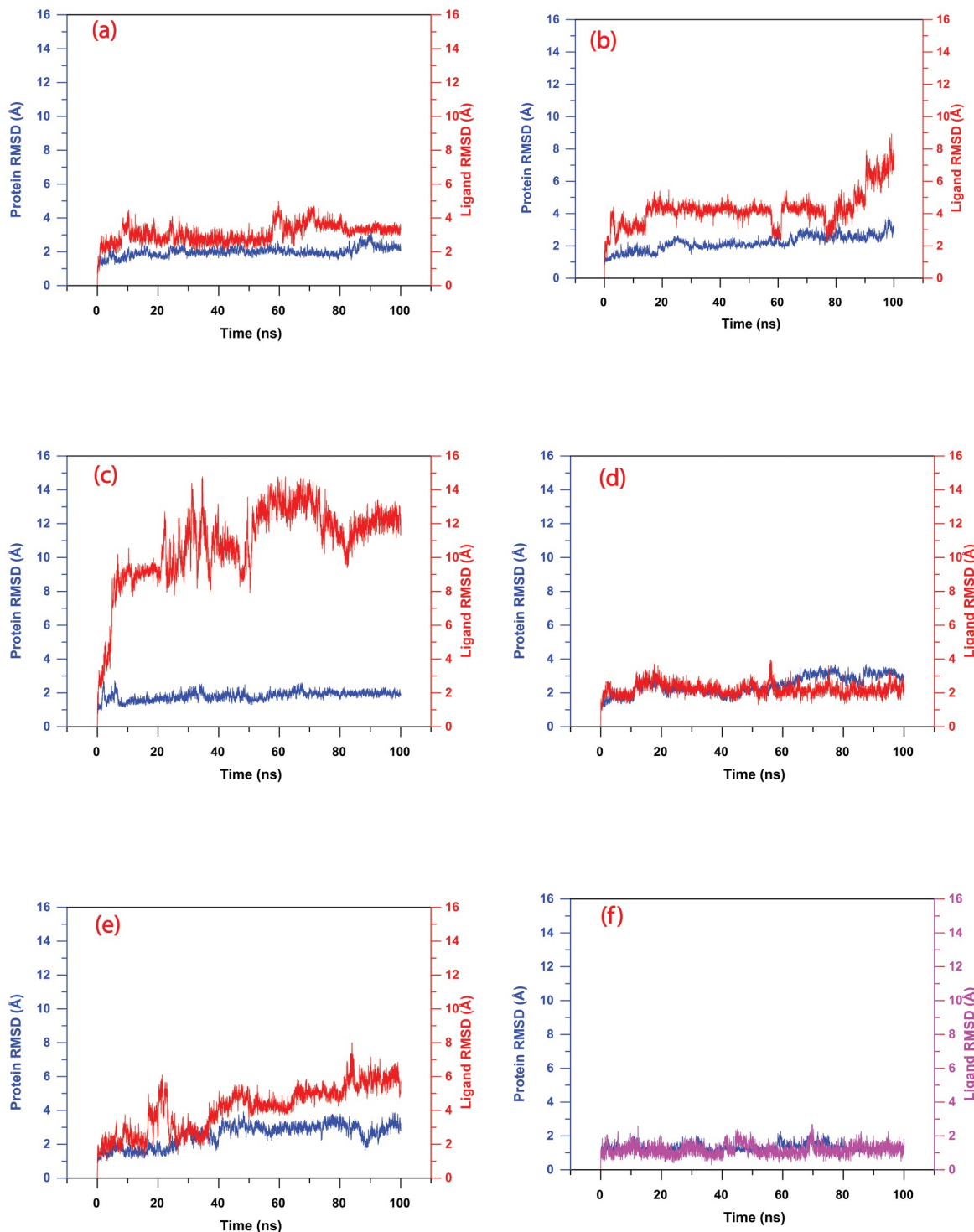


Fig 7. Root mean square deviation (RMSD) plots for (a) M^{pro}-CHEMBL1940602 (b) M^{pro}-CHEMBL2036486 (c) M^{pro}-CHEMBL3628485 (d) M^{pro}-CHEMBL200972 (e) M^{pro}-CHEMBL2036488, and (f) M^{pro}-X77 (control), calculated over the period of 100 ns MD simulation.

<https://doi.org/10.1371/journal.pone.0277328.g007>

(protein and ligand) are parallel to the X-axis demonstrates their higher conformational stability. CHEMBL200972 showed the minimum deviation (<3 Å) pattern among the screened compounds and attained stability at the very early stage of the simulation. Also, CHEMBL1940602 took 10 ns to reach stability, exhibited a steady pattern and showed an overall deviation of less than 4 Å. It deviated at 10 ns and between 60 to 80 ns up to 4 Å, and then it came down to attain the equilibrium at 3 Å. Among all the screened compounds, CHEMBL3628485 showed the highest deviation up to 14 Å which cannot be considered as an acceptable RMSD. The translation motion of CHEMBL3628485 was also observed in the first and last pose obtained from simulation (Fig 6), confirming its higher dynamic instability. These compounds deviated up to 8 Å as soon as the simulation started and never attained a stable trajectory ending with a maximum deviation at ≥ 14 Å accompanied by continuous fluctuation till the end of the simulation. This clearly suggests that the compound is not stable at the binding site, and a more extended simulation (> 100 ns) would be required to understand the behaviour of CHEMBL3628485. Compound CHEMBL2036486 had a stable trajectory for the initial 75 ns of simulation; however, it showed deviation up to > 8 Å. Like CHEMBL3628485, CHEMBL2036486 would also be required longer (> 100 ns) simulation studies to understand whether it is stable in the binding pocket of protein or not. However, in the case of CHEMBL2036488, the deviation is not high as CHEMBL3628485 but also not stable as CHEMBL1940602, CHEMBL200972, and control compound complexes. Here, it deviated to RMSD greater than 4 Å after 40 ns of simulation time and then further deviated to 6 Å during the last 20 ns of simulation. In conclusion, compared to the control, the dynamic stability shown by the screened was in the decreasing order of CHEMBL200972, CHEMBL1940602, CHEMBL2036486, CHEMBL2036488, and CHEMBL3628485.

3.5.2 Root Mean Square Fluctuation (RMSF). As noted previously, protein exhibited a steady pattern; therefore, none of the complexes exhibited abrupt RMSF behaviour, as illustrated in **S1 Fig in S1 File**. Protein RMSF values were calculated for the $\text{C}\alpha$ atoms of each residue. All residues from M^{PRO} showed stable RMSF < 3 Å in all the complexes. Only in the CHEMBL200972 docked complex, there was a single relatively higher peak shown for Ala194 where RMSF > 3 Å. The control compound among all the docked complexes showed the most stable pattern for all the protein residues. None of the key residues displayed a substantial conformational change in this instance. This reflects the stability of the protein in the protein-ligand complex.

3.6 Binding free energy calculation

To assess the stability of the complex in MD simulation, the binding free energy of MM/GBSA was computed throughout the 100 ns trajectory. Table 2 shows the MM/GBSA binding free

Table 2. MM/GBSA binding energy components for selected and control compounds.

MM/GBSA components	CHEMBL1940602	CHEMBL2036486	CHEMBL3628485	CHEMBL200972	CHEMBL2036488	Control (X77 inhibitor)
ΔG_{Bind}	-64.72 \pm 9.23	-70.13 \pm 10.00	-40.89 \pm 11.28	-88.98 \pm 8.95	-72.84 \pm 11.53	-64.53 \pm 7.26
$\Delta G_{\text{Bind Coulomb}}$	-2.82 \pm 38.59	-28.23 \pm 8.04	-85.21 \pm 25.94	-115.93 \pm 23.70	-26.07 \pm 7.48	-33.01 \pm 25.05
$\Delta G_{\text{Bind Covalent}}$	7.10 \pm 2.27	2.30 \pm 2.95	3.46 \pm 2.62	8.12 \pm 2.83	3.09 \pm 4.20	3.52 \pm 1.83
$\Delta G_{\text{Bind Hbond}}$	-1.55 \pm 1.10	-2.30 \pm 0.76	-2.94 \pm 1.17	-4.38 \pm 0.58	-2.04 \pm 0.66	-1.88 \pm 0.37
$\Delta G_{\text{Bind Lipo}}$	-19.86 \pm 1.64	-16.10 \pm 2.28	-9.28 \pm 2.89	-19.47 \pm 1.77	-17.28 \pm 2.95	-14.58 \pm 1.11
$\Delta G_{\text{Bind Packing}}$	-2.59 \pm 0.58	-2.23 \pm 0.78	-0.73 \pm 0.87	-1.93 \pm 0.69	-2.39 \pm 0.89	-1.24 \pm 0.44
$\Delta G_{\text{Bind Solv GB}}$	17.76 \pm 34.60	32.56 \pm 5.15	85.51 \pm 22.06	109.30 \pm 21.63	33.54 \pm 5.12	33.52 \pm 19.90
$\Delta G_{\text{Bind vdW}}$	-76.30 \pm 3.72	-56.04 \pm 5.69	-31.83 \pm 7.58	-65.33 \pm 4.32	-61.69 \pm 7.77	-50.86 \pm 2.85
StrainEnergy	7.14 \pm 2.499	9.10 \pm 3.75	6.55 \pm 4.25	14.17 \pm 2.93	12.28 \pm 4.50	5.99 \pm 2.61

<https://doi.org/10.1371/journal.pone.0277328.t002>

energy of all five compounds and the control compound. ΔG_{bind} is minimum for CHEMBL200972 that shows it maximum binding affinity, -88.98 kcal/mol with M^{Pro} . However, CHEMBL2036486 (-70.13 kcal/mole) and CHEMBL2036488 (-72.84 kcal/mol) showed better performance than control and were considered relatively acceptable complexes as compared to the control compound-complex. Compound CHEMBL1940602 and control exhibited similar ΔG_{bind} (-64.72 and -64.53 kcal/mol); thus, they cannot be differentiated. Furthermore, MM/GBSA data showed that CHEMBL3628485 had relatively poor binding (-40.89 kcal/mol) with M^{Pro} ; thus, the compound is not highly stable at the protein's binding site. Van der Waal interaction was the major contributor to binding free energy for CHEMBL1940602 (-76.30 kcal/mol), CHEMBL2036486 (-56.04 kcal/mol), CHEMBL2036488 (-61.69 kcal/mol) and control (-50.86 kcal/mol). In contrast, CHEMBL3628485 and CHEMBL200972 were maximally stabilised by coulombic interaction with -85.21 kcal/mol and -115.93 kcal/mol energies, respectively. The best H-bond energy was found best in compound CHEMBL200972 at -4.38 kcal/mol, followed by CHEMBL3628485, CHEMBL2036486, CHEMBL2036488, control, and CHEMBL1940602 at -2.94 kcal/mol, -2.30 kcal/mol, -2.04 kcal/mol, -1.88 kcal/mol, and -1.55 kcal/mol, respectively.

3.7 Interactive residues in MD trajectory

Residues that showed interaction with protein in their best-docked poses were also analysed for their interaction over the period of 100 ns of simulation. Compound CHEMBL1940602 had a stacking interaction with catalytic dyad residue His41, which was retained for 58% of the simulation time. However, water-mediated H-bonds by Asp187 and His164 were shown for 91% and 64%, respectively. Here, H-bond interaction with Asp¹⁸⁷ is a strong indicator for the stabilization of CHEMBL1940602 in the binding site of M^{Pro} . In compound CHEMBL2036486, Glu166 formed a water bridge with the ligand's hydroxyl group and had a maximum occurrence frequency of 74% during the simulation. CHEMBL3628485 formed H-bonds with Glu47 and Glu166, but the frequency of occurrence was < 60% in both cases, indicating that CHEMBL3628485 has lower interaction stability with the pocket lining residue of M^{Pro} . In contrast, CHEMBL200972 had several H-bond interactions where the frequency of occurrence was > 60%, especially with the residue Glu166 (84%, 72%, 72%, 87% and 81%), His164 (69%) and Gln189 (76%). Glu166 was found as a crucial residue in the experimental co-complex of the native ligand with the protein. This indicates the higher stability of CHEMBL200972 within the binding site of M^{Pro} .

Similarly, the CHEMBL2036488 complex also had Glu166, and His163 which showed H-bonds with ligand for more than 60% of the entire frame (60% and 70%). This also indicated a higher and relevant binding stability of CHEMBL2036488 at the protein's binding site. Protein-ligand interaction and percentage of occurrence over the 100 ns simulation trajectory is shown in [Fig 8](#) and [S2 Fig in S1 File](#). As it can be observed in [Fig 8\(f\)](#), the control ligand started showing H-bond with Gly143 for 86% of the total time frame, which was missing in the rigid docked complex. The control compound also showed a considerable binding with Glu166 with a 94% frequency of occurrence of H-bonds. His163, a critical contact in the native ligand in the crystal structure ([Fig 2](#)), was also missing from the docked complex of control ([Fig 5\(f\)](#)). However, it gained access to the ligand during simulation, and [Fig 8\(f\)](#) shows the His163 with 93% of the time involved in H-bond.

3.8 Principal component analysis

PCA is utilised to handle the high dimensional movement of the system by minimising its space during the MD simulation trajectory. This was achieved by transforming every set of

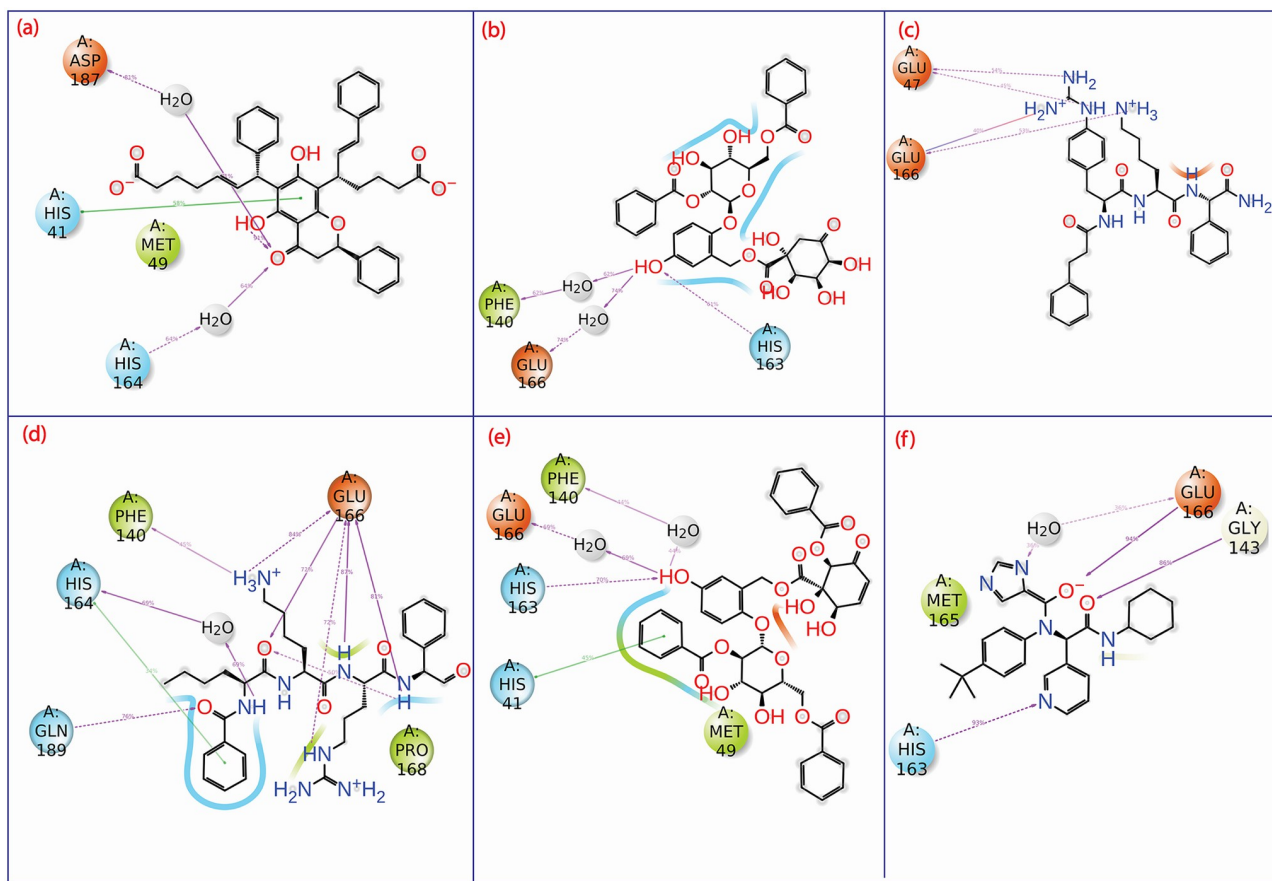


Fig 8. 2D interaction diagram of protein-ligand interactions maps for (a) M^{Pro}-CHEMBL1940602 (b) M^{Pro}-CHEMBL2036486 (c) M^{Pro}-CHEMBL3628485 (d) M^{Pro}-CHEMBL200972 (e) M^{Pro}-CHEMBL2036488, and (f) M^{Pro}-X77 (control), over the 100 ns MD simulation.

<https://doi.org/10.1371/journal.pone.0277328.g008>

associated atomic motions into a collection and assessment of principal components. These principal components are the true representatives of the motion of the biological system during the MD simulation. The PCA was used to evaluate the association between statistically significant conformational variations created during the MD simulation. This study considered the first three principal components to show the conformational variation. Compound CHEMBL1940602 showed a 61.9% cumulative variation for the top 3 PCAs. Similarly, for compounds CHEMBL2036486, CHEMBL3628485, CHEMBL200972, CHEMBL2036488, and control, the top 3 PCAs constituted 66.7%, 59.7%, 61.2%, 63.8% and 45.56%, respectively. Fig 9 shows the top 3 PCA for all 5 compounds and control. Here, each dot represents the conformation of a protein. The spread of different colours in the plot depicts the degree of conformational change. However, the change in colour (blue to white to red) represents the simulation's initial, intermediate, and final time step. Fig 9(a2) shows the first two principal component analyses for CHEMBL1940602 with a wide range of data points that reflect the degree of conformational changes recorded during the simulation.

Moreover, the data points were found continuous in CHEMBL1940602 for all the PCs plots that showed the constant conformational change. The conformation of compound CHEMBL2036486 varied similarly, but there was a non-overlapping subspace in the PC1-PC2 plot that indicated the distinct periodic jump. Compounds CHEMBL3628485, CHEMBL2036488, and control showed similar patterns of uniform conformational change.

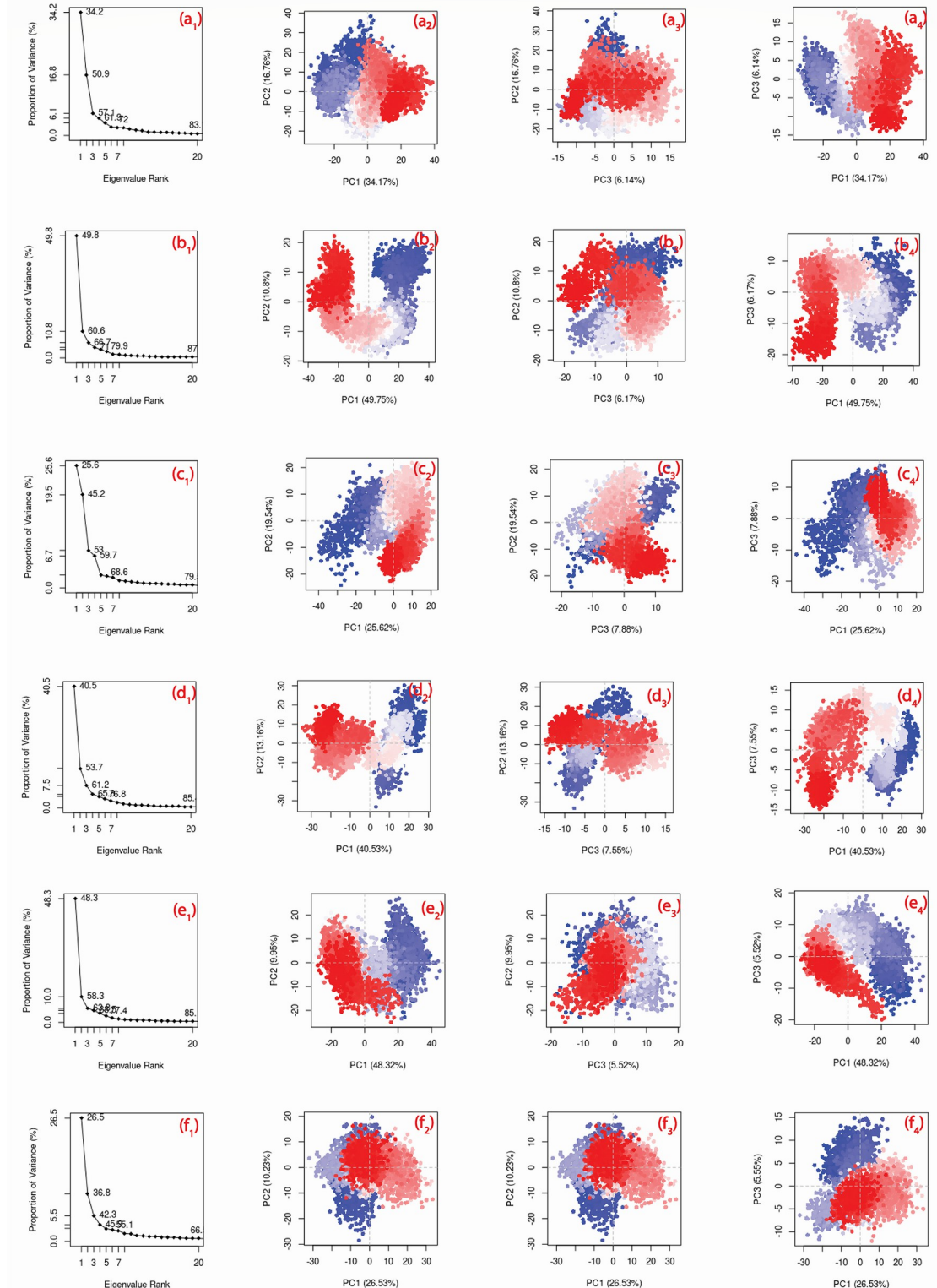


Fig 9. Principal component cluster analysis along first three PCs for (a1-a4) CHEMBL1940602, (b1-b4) CHEMBL2036486, (c1-c4) CHEMBL3628485, (d1-d4) CHEMBL200972, (e1-e4) CHEMBL2036488 and (f1-f4) X77 (control). The spread of dots represents the degree of conformational change while the colour code represents the time steps (blue: initial, white: intermediate and red: final).

<https://doi.org/10.1371/journal.pone.0277328.g009>

However, the uniformity was maximum in the control case. Compound CHEMBL200972 showed a relatively lesser distribution in the PC1-PC2 plot, which indicates a lower degree of conformational change.

In each docked complex, M^{PRO} structures show a significant drop in variance about the first three eigenmodes, suggesting that docked ligands have induced conformational motion. The variance was followed by the elbow point, but no further significant changes in eigen fraction were observed after 4 to 20 eigen values (Fig 9). This observation suggested that the initial stages of simulation showed considerable flexibility in protein structure docked with respective ligands, but this flexibility reduced with simulation intervals. It is further suggested that the local fluctuations in M^{PRO} structure in each docked complex tend to stabilize with time, as is suggested by the decreasing percentage of eigen modes. Previous studies have observed similar results with fructose transporter GLUT5 and G-protein-coupled receptor 119 docked with their respective ligands [79, 80].

Three PCs or eigen vectors for M^{PRO} docked with selected putative compounds and X77 (control) were extracted from the respective MD trajectories and represented in clusters (Fig 9). The analysis of all three PCs supported the compact-cluster motions in Mpro in respective complexes during the MD simulation. Overall, the coupled motion in Mpro structure across all the system demonstrated the stiffness and significant fluctuations induced at the active site on binding of selected ligands during the simulation. Hence the overall observations suggested the stability of selected compounds i.e., CHEMBL1940602, CHEMBL2036486, CHEMBL3628485, CHEMBL200972, and CHEMBL2036488 against X77 inhibitor in the Mpro active pocket, and finally restricting the essential motion of protein required for enzymatic function, leading to its inhibition.

4. Discussions

This work demonstrates the structure-based screening of anti-dengue drugs against the SARS-CoV-2 M^{PRO} . In SARS-CoV-2, the main protease (M^{PRO}) is responsible for the maturation of polyprotein, which is essential for the virus's proliferation [20]. In addition, M^{PRO} also plays a role in the proteolytic processing of enzymes required for the replication of SARS-CoV-2 [81, 82]. This makes M^{PRO} an essential pharmacological target for suppressing SARS-CoV-2 proliferation, which contains the catalytic dyad (Cys145 and His41) in a substrate binding cleft required for its catalytic function. The virtual screening of experimentally validated 330 anti-dengue compounds known for their antiviral activity resulted in the identification of potential Mpro active site binders named CHEMBL1940602, CHEMBL2036486, CHEMBL3628485, CHEMBL200972, and CHEMBL2036488. The computational approaches such as high throughput virtual screening, molecular docking, and molecular dynamic simulation, were implemented in this study for the in-silico characterization of known anti-DENV compounds against SARS-CoV-2 M^{PRO} . The results obtained from all these computational experiments were compared to the control M^{PRO} ligand, i.e. X77, derived from the crystal structure of SARS-CoV-2 Mpro (PDB ID:6W63). The amino acids Gly143, Glu166, Cys145, and His163 are reported as critical binding site residues involved in forming H-bonds with the ligand [41], which was also observed in the case of the control ligand (X77), found to form H-bonds with Gly143 and Glu166. The substrate binding site consists of four subsites S1', S1, S2, and S4, [24–28] and the binding of chemical compounds to these subsites leads to the inhibition of M^{PRO} .

A catalytic dyad (Cys145 and His41) creates a nucleophilic reaction required for the proteolytic cleavage [83] in which a proton is translocated from Cys145 to His41 due to simultaneous nucleophilic attack on the peptide carbonyl carbon by the sulfur atom of Cys145. Further, the

proton from His145 is translocated to the substrate nitrogen atom resulting in the formation of acyl-enzyme complex intermediate, which assists peptide cleavage [84, 85].

The Initial docking poses for all screened compounds showed that Glu166 had been observed as a potential hydrogen bond formation residue in four of five selected compounds. Glu166 has also been reported to interact with protease inhibitors such as telaprevir, boceprevir, and narnavir in the case of HCV NS3/4A proteolytic cleavage [86]. The alignment of earlier findings with the outcome of this study indicates the possible inhibitory activities of screened compounds (CHEMBL2036486, CHEMBL3628485, CHEMBL200972, and CHEMBL2036488). However, a protein-ligand complex containing CHEMBL1940602 showed the involvement of Asn142 in forming H-bonds. An earlier study found that Asn142 was in the list of residues that formed H-bonds with 17 Marine Natural Products, which were found to be M^{pro} inhibitors [87].

Additionally, Gly143 was reported as the most potent residue to form H-bonds [41], and this study showed its presence in the complex containing CHEMBL1940602 as an H-bond acceptor. Compound CHEMBL2036488 formed π - π interaction with catalytic residue His41. This interaction was also reported in the case of baicalein, which exhibited a distinctive interaction pattern with SARS-CoV-2-M^{pro} [88].

The best-docked poses of all five screened compounds were further analysed for their dynamic stability within the docked complex via MD simulation. In all the docked complexes, the α -Carbon atoms of SARS-CoV-2 M^{pro} showed fluctuations in the considered range (< 3 Å) compared to the control docked complex. Furthermore, All protein fit ligands except CHEMBL3628485 showed a stable trajectory with an RMSD value (< 3 Å) which is considered highly stable as reported in several previous studies [89–91]. Protein-ligand interaction study over the simulation period confirmed that most of the interactions shown in the docked poses were retained during the MD simulation. Glu166 was the most common residue that showed interaction in the case of all the screened compounds except CHEMBL1940602 over the entire simulation trajectory. The compound CHEMBL200972 showed the most stable trajectory and formed an H-bond with Glu166 as the maximum number of simulation frames. Along with the high dynamic stability, the binding free energy of CHEMBL200972 was -88.98 ± 8.95 kcal/mole, which proved it the most energetically stable compound among all protein-ligand complexes over the 100 ns simulation. However, the remaining four molecules also showed relevant ΔG values compared to the control molecule (X77).

5. Conclusion

The Repositioning of anti-dengue compounds against SARS-CoV-2 M^{pro} could facilitate the discovery of potential anti-SARS-CoV-2 therapeutics. This study showed a rapid method to screen a library of 330 anti-dengue compounds against the substrate binding site of SARS-CoV-2 M^{pro}. It evaluated the findings by comparing them with Crystal ligand structure (PDB ID: 6W63) X77. Based on the docking score (< 10.0 kcal/mol), the top 5 compounds; a) Characeone D (CHEMBL1940602) (b) Flacourtoside D (CHEMBL2036486), (c) deamino-Phe-Phe (4-guanidino)-Lys-Phg-NH₂ (CHEMBL3628485) (d) Bz-Nle-Lys-Arg-Phg-al (CHEMBL200972) and (e) Flacourtoside F (CHEMBL2036488) were selected for intermolecular interaction studies, structural stability analysis and binding free energy calculations. The best docked poses of these compounds have shown interactions with one or more active site residues His41, Asn142, Gly143, Cys145, His163 and Glu166 of M^{pro}. Further, the dynamic stability of each protein-ligand complex was estimated using 100 ns MD simulation, where CHEMBL200972 has shown maximum dynamic stability with minimum fluctuation over the 100 ns MD trajectory. All five compounds' MM/GBSA binding energies were better compared to the

control molecule (X77). Complimenting to the MD simulation results, CHEMBL200972 showed the best ΔG score making it a potential hit for M^{PRO} . By directly interacting with the substrate binding residues of M^{PRO} , these five compounds may block the polyprotein processing of SARS-CoV-2. These hits also showed π - π interaction with His41, an essential catalytic residue for M^{PRO} that helps create the nucleophilic environment to assist natural substrate binding. Any interaction with His 41 can alter the binding site's nature, further inhibiting the polyprotein processing. In order to assess the potential of the top five screened compounds, the Computational findings of this study need to be validated in an

Supporting information

S1 File.

(DOCX)

S2 File.

(DOCX)

Acknowledgments

The authors are highly thankful to Dr. Amaresh Kumar Sahoo, Indian Institute of Information Technology, Prayagraj, India for providing his kind support for giving access to Schrödinger suite (Virtual screening workflow & MMGSA).

Author Contributions

Conceptualization: Leena H. Bajrai, Vivek Dhar Dwivedi, Esam I. Azhar.

Data curation: Leena H. Bajrai, Arwa A. Faizo, Areej A. Alkhaldy, Vivek Dhar Dwivedi.

Formal analysis: Leena H. Bajrai, Arwa A. Faizo, Areej A. Alkhaldy, Vivek Dhar Dwivedi.

Investigation: Vivek Dhar Dwivedi, Esam I. Azhar.

Methodology: Leena H. Bajrai, Arwa A. Faizo, Areej A. Alkhaldy, Vivek Dhar Dwivedi, Esam I. Azhar.

Software: Leena H. Bajrai, Arwa A. Faizo, Areej A. Alkhaldy, Vivek Dhar Dwivedi.

Supervision: Vivek Dhar Dwivedi, Esam I. Azhar.

Validation: Leena H. Bajrai, Vivek Dhar Dwivedi, Esam I. Azhar.

Visualization: Leena H. Bajrai, Arwa A. Faizo, Areej A. Alkhaldy, Vivek Dhar Dwivedi.

Writing – original draft: Leena H. Bajrai, Vivek Dhar Dwivedi.

Writing – review & editing: Leena H. Bajrai, Vivek Dhar Dwivedi, Esam I. Azhar.

References

1. Keni R, Alexander A, Nayak PG, Mudgal J, Nandakumar K. COVID-19: Emergence, Spread, Possible Treatments, and Global Burden. *Front Public Health*. 2020; 8: 216. <https://doi.org/10.3389/fpubh.2020.00216> PMID: 32574299
2. Wu C, Liu Y, Yang Y, Zhang P, Zhong W, Wang Y, et al. Analysis of therapeutic targets for SARS-CoV-2 and discovery of potential drugs by computational methods. *Acta Pharm Sin B*. 2020; 10: 766–788. <https://doi.org/10.1016/j.apsb.2020.02.008> PMID: 32292689
3. Liu C, Zhou Q, Li Y, Garner LV, Watkins SP, Carter LJ, et al. Research and Development on Therapeutic Agents and Vaccines for COVID-19 and Related Human Coronavirus Diseases. *ACS Cent Sci*. 2020; 6: 315–331. <https://doi.org/10.1021/acscentsci.0c00272> PMID: 32226821

4. Yadav R, Chaudhary JK, Jain N, Chaudhary PK, Khanra S, Dhamija P, et al. Role of Structural and Non-Structural Proteins and Therapeutic Targets of SARS-CoV-2 for COVID-19. *Cells*. 2021; 10: 821. <https://doi.org/10.3390/cells10040821> PMID: 33917481
5. Shyr ZA, Gorshkov K, Chen CZ, Zheng W. Drug Discovery Strategies for SARS-CoV-2. *J Pharmacol Exp Ther*. 2020; 375: 127–138. <https://doi.org/10.1124/jpet.120.000123> PMID: 32723801
6. Kim C, Mahasenan KV, Bhardwaj A, Wiest O, Chang M, Mobashery S. Production of Proteins of the SARS-CoV-2 Proteome for Drug Discovery. *ACS Omega*. 2021; 6: 19983–19994. <https://doi.org/10.1021/acsomega.1c02984> PMID: 34337272
7. Maia EHB, Assis LC, de Oliveira TA, da Silva AM, Taranto AG. Structure-Based Virtual Screening: From Classical to Artificial Intelligence. *Front Chem*. 2020; 8: 343. <https://doi.org/10.3389/fchem.2020.00343> PMID: 32411671
8. Hughes JP, Rees S, Kalindjian SB, Philpott KL. Principles of early drug discovery. *Br J Pharmacol*. 2011; 162: 1239–1249. <https://doi.org/10.1111/j.1476-5381.2010.01127.x> PMID: 21091654
9. Lionta E, Spyrou G, Vassilatis DK, Cournia Z. Structure-based virtual screening for drug discovery: principles, applications and recent advances. *Curr Top Med Chem*. 2014; 14: 1923–1938. <https://doi.org/10.2174/1568026614666140929124445> PMID: 25262799
10. Sharma A, Gupta SP. Fundamentals of Viruses and Their Proteases. *Viral Proteases and Their Inhibitors*. Elsevier; 2017. pp. 1–24. <https://doi.org/10.1016/B978-0-12-809712-0.00001-0>
11. Gioia M, Ciaccio C, Calligari P, De Simone G, Sbardella D, Tundo G, et al. Role of proteolytic enzymes in the COVID-19 infection and promising therapeutic approaches. *Biochem Pharmacol*. 2020; 182: 114225. <https://doi.org/10.1016/j.bcp.2020.114225> PMID: 32956643
12. Seth S, Batra J, Srinivasan S. COVID-19: Targeting Proteases in Viral Invasion and Host Immune Response. *Front Mol Biosci*. 2020; 7: 215. <https://doi.org/10.3389/fmolsb.2020.00215> PMID: 33195400
13. Craik CS, Page MJ, Madison EL. Proteases as therapeutics. *Biochem J*. 2011; 435: 1–16. <https://doi.org/10.1042/BJ20100965> PMID: 21406063
14. Narayanan A, Narwal M, Majowicz SA, Varricchio C, Toner SA, Ballatore C, et al. Identification of SARS-CoV-2 inhibitors targeting Mpro and PLpro using in-cell-protease assay. *Commun Biol*. 2022; 5: 169. <https://doi.org/10.1038/s42003-022-03090-9> PMID: 35217718
15. Cui W, Yang K, Yang H. Recent Progress in the Drug Development Targeting SARS-CoV-2 Main Protease as Treatment for COVID-19. *Front Mol Biosci*. 2020; 7: 616341. <https://doi.org/10.3389/fmolsb.2020.616341> PMID: 33344509
16. Wang Y, Lv Z, Chu Y. HIV protease inhibitors: a review of molecular selectivity and toxicity. *HIV/AIDS—Res Palliat Care*. 2015; 95. <https://doi.org/10.2147/HIV.S79956> PMID: 25897264
17. de Leuw P, Stephan C. Protease inhibitors for the treatment of hepatitis C virus infection. *GMS Infect Dis* 5Doc08. 2017 [cited 23 May 2022].
18. Gorbatenya AE, Koonin EV, Donchenko AP, Blinov VM. Coronavirus genome: prediction of putative functional domains in the non-structural polyprotein by comparative amino acid sequence analysis. *Nucleic Acids Res*. 1989; 17: 4847–4861. <https://doi.org/10.1093/nar/17.12.4847> PMID: 2526320
19. Lee H-J, Shieh C-K, Gorbatenya AE, Koonin EV, La Monica N, Tuler J, et al. The complete sequence (22 kilobases) of murine coronavirus gene 1 encoding the putative proteases and RNA polymerase. *Virology*. 1991; 180: 567–582. [https://doi.org/10.1016/0042-6822\(91\)90071-i](https://doi.org/10.1016/0042-6822(91)90071-i) PMID: 1846489
20. Gorbatenya AE, Snijder EJ, Ziebuhr J. Virus-encoded proteinases and proteolytic processing in the Nidovirales. *J Gen Virol*. 2000; 81: 853–879. <https://doi.org/10.1099/0022-1317-81-4-853> PMID: 10725411
21. Xue X, Yu H, Yang H, Xue F, Wu Z, Shen W, et al. Structures of two coronavirus main proteases: implications for substrate binding and antiviral drug design. *J Virol*. 2008; 82: 2515–2527. <https://doi.org/10.1128/JVI.02114-07> PMID: 18094151
22. Ren Z, Yan L, Zhang N, Guo Y, Yang C, Lou Z, et al. The newly emerged SARS-like coronavirus HCoV-EMC also has an “Achilles’ heel”: current effective inhibitor targeting a 3C-like protease. *Protein Cell*. 2013; 4: 248–250. <https://doi.org/10.1007/s13238-013-2841-3> PMID: 23549610
23. Wang F, Chen C, Tan W, Yang K, Yang H. Structure of Main Protease from Human Coronavirus NL63: Insights for Wide Spectrum Anti-Coronavirus Drug Design. *Sci Rep*. 2016; 6: 22677. <https://doi.org/10.1038/srep22677> PMID: 26948040
24. Linlin Z, Daizong L, Xinyuanyuan S, Ute C, Christian Dr LS, Stephan B, et al. Crystal structure of SARS-CoV-2 main protease provides a basis for design of improved α -ketoamide inhibitors. *Science*. 2020; 368.
25. Yang H, Yang M, Ding Y, Liu Y, Lou Z, Zhou Z, et al. The crystal structures of severe acute respiratory syndrome virus main protease and its complex with an inhibitor. *Proc Natl Acad Sci*. 2003; 100: 13190–13195. <https://doi.org/10.1073/pnas.1835675100> PMID: 14585926

26. Hsu M-F, Kuo C-J, Chang K-T, Chang H-C, Chou C-C, Ko T-P, et al. Mechanism of the Maturation Process of SARS-CoV 3CL Protease*[boxs]. *J Biol Chem*. 2005; 280: 31257–31266.
27. Chou C-Y, Chang H-C, Hsu W-C, Lin T-Z, Lin C-H, Chang G-G. Quaternary structure of the severe acute respiratory syndrome (SARS) coronavirus main protease. *Biochemistry*. 2004; 43: 14958–14970. <https://doi.org/10.1021/bi0490237> PMID: 15554703
28. ul Qamar MT, Alqahtani SM, Alamri MA, Chen L-L. Structural basis of SARS-CoV-2 3CLpro and anti-COVID-19 drug discovery from medicinal plants. *J Pharm Anal*. 2020; 10: 313–319. <https://doi.org/10.1016/j.jpha.2020.03.009> PMID: 32296570
29. Grum-Tokars V, Ratia K, Begaye A, Baker SC, Mesecar AD. Evaluating the 3C-like protease activity of SARS-CoV-2: recommendations for standardized assays for drug discovery. *Virus Res*. 2008; 133: 63–73. <https://doi.org/10.1016/j.virusres.2007.02.015> PMID: 17397958
30. Pillaiyar T, Manickam M, Namasivayam V, Hayashi Y, Jung S-H. An overview of severe acute respiratory syndrome–coronavirus (SARS-CoV) 3CL protease inhibitors: peptidomimetics and small molecule chemotherapy. *J Med Chem*. 2016; 59: 6595–6628. <https://doi.org/10.1021/acs.jmedchem.5b01461> PMID: 26878082
31. Kneller DW, Phillips G, Weiss KL, Zhang Q, Coates L, Kovalevsky A. Direct Observation of Protonation State Modulation in SARS-CoV-2 Main Protease upon Inhibitor Binding with Neutron Crystallography. *J Med Chem*. 2021; 64: 4991–5000. <https://doi.org/10.1021/acs.jmedchem.1c00058> PMID: 33755450
32. Sepay N, Saha PC, Shahzadi Z, Chakraborty A, Halder UC. A crystallography-based investigation of weak interactions for drug design against COVID-19. *Phys Chem Chem Phys*. 2021; 23: 7261–7270. <https://doi.org/10.1039/d0cp05714b> PMID: 33876086
33. Morselli Gysi D, do Valle I, Zitnik M, Ameli A, Gan X, Varol O, et al. Network medicine framework for identifying drug-repurposing opportunities for COVID-19. *Proc Natl Acad Sci*. 2021; 118: e2025581118. <https://doi.org/10.1073/pnas.2025581118> PMID: 33906951
34. Bárcena M, Barnes CO, Beck M, Bjorkman PJ, Canard B, Gao GF, et al. Structural biology in the fight against COVID-19. *Nat Struct Mol Biol*. 2021; 28: 2–7. <https://doi.org/10.1038/s41594-020-00544-8> PMID: 33437043
35. Zhang S, Krumberger M, Morris MA, Parrocha CMT, Kreutzer AG, Nowick JS. Structure-based drug design of an inhibitor of the SARS-CoV-2 (COVID-19) main protease using free software: A tutorial for students and scientists. *Eur J Med Chem*. 2021; 218: 113390. <https://doi.org/10.1016/j.ejmech.2021.113390> PMID: 33812315
36. Acharya A, Agarwal R, Baker MB, Baudry J, Bhowmik D, Boehm S, et al. Supercomputer-Based Ensemble Docking Drug Discovery Pipeline with Application to Covid-19. *J Chem Inf Model*. 2020; 60: 5832–5852. <https://doi.org/10.1021/acs.jcim.0c01010> PMID: 33326239
37. Ma C, Sacco MD, Hurst B, Townsend JA, Hu Y, Szeto T, et al. Boceprevir, GC-376, and calpain inhibitors II, XII inhibit SARS-CoV-2 viral replication by targeting the viral main protease. *Cell Res*. 2020; 30: 678–692. <https://doi.org/10.1038/s41422-020-0356-z> PMID: 32541865
38. Ghahremanpour MM, Tirado-Rives J, Deshmukh M, Ippolito JA, Zhang C-H, Cabeza de Vaca I, et al. Identification of 14 Known Drugs as Inhibitors of the Main Protease of SARS-CoV-2. *ACS Med Chem Lett*. 2020; 11: 2526–2533. <https://doi.org/10.1021/acsmedchemlett.0c00521> PMID: 33324471
39. Douangamath A, Fearon D, Gehrtz P, Krojer T, Lukacik P, Owen CD, et al. Crystallographic and electrophilic fragment screening of the SARS-CoV-2 main protease. *Nat Commun*. 2020; 11: 5047. <https://doi.org/10.1038/s41467-020-18709-w> PMID: 33028810
40. Panda PK, Arul MN, Patel P, Verma SK, Luo W, Rubahn H-G, et al. Structure-based drug designing and immunoinformatics approach for SARS-CoV-2. *Sci Adv*. 2020; 6: eabb8097. <https://doi.org/10.1126/sciadv.abb8097> PMID: 32691011
41. Nguyen DD, Gao K, Chen J, Wang R, Wei G-W. Unveiling the molecular mechanism of SARS-CoV-2 main protease inhibition from 137 crystal structures using algebraic topology and deep learning. *Chem Sci*. 2020; 11: 12036–12046. <https://doi.org/10.1039/d0sc04641h> PMID: 34123218
42. Kneller DW, Phillips G, O'Neill HM, Jedrzejczak R, Stols L, Langan P, et al. Structural plasticity of SARS-CoV-2 3CL M^{pro} active site cavity revealed by room temperature X-ray crystallography. *Nat Commun*. 2020; 11: 3202. <https://doi.org/10.1038/s41467-020-16954-7> PMID: 32581217
43. Cho E, Rosa M, Anjum R, Mehmood S, Soban M, Mujtaba M, et al. Dynamic Profiling of β-Coronavirus 3CL M^{pro} Protease Ligand-Binding Sites. *J Chem Inf Model*. 2021; 61: 3058–3073. <https://doi.org/10.1021/acs.jcim.1c00449> PMID: 34124899
44. Su H, Zhou F, Huang Z, Ma X, Natarajan K, Zhang M, et al. Molecular Insights into Small-Molecule Drug Discovery for SARS-CoV-2. *Angew Chem Int Ed*. 2021; 60: 9789–9802. <https://doi.org/10.1002/anie.202008835> PMID: 32729180

45. Li Z, Li X, Huang Y-Y, Wu Y, Liu R, Zhou L, et al. Identify potent SARS-CoV-2 main protease inhibitors via accelerated free energy perturbation-based virtual screening of existing drugs. *Proc Natl Acad Sci.* 2020; 117: 27381–27387. <https://doi.org/10.1073/pnas.2010470117> PMID: 33051297
46. Kneller DW, Galanis S, Phillips G, O'Neill HM, Coates L, Kovalevsky A. Malleability of the SARS-CoV-2 3CL Mpro Active-Site Cavity Facilitates Binding of Clinical Antivirals. *Structure.* 2020; 28: 1313–1320. e3. <https://doi.org/10.1016/j.str.2020.10.007> PMID: 33152262
47. Jin Z, Du X, Xu Y, Deng Y, Liu M, Zhao Y, et al. Structure of Mpro from SARS-CoV-2 and discovery of its inhibitors. *Nature.* 2020; 582: 289–293. <https://doi.org/10.1038/s41586-020-2223-y> PMID: 32272481
48. Luttens A, Gullberg H, Abdurakhmanov E, Vo DD, Akaber D, Talibov VO, et al. Ultralarge Virtual Screening Identifies SARS-CoV-2 Main Protease Inhibitors with Broad-Spectrum Activity against Coronaviruses. *J Am Chem Soc.* 2022; 144: 2905–2920. <https://doi.org/10.1021/jacs.1c08402> PMID: 35142215
49. Kumar BK, Faheem, Sekhar KVGC, Ojha R, Prajapati VK, Pai A, et al. Pharmacophore based virtual screening, molecular docking, molecular dynamics and MM-GBSA approach for identification of prospective SARS-CoV-2 inhibitor from natural product databases. *J Biomol Struct Dyn.* 2022; 40: 1363–1386. <https://doi.org/10.1080/07391102.2020.1824814> PMID: 32981461
50. Elseginy SA. Virtual screening and structure-based 3D pharmacophore approach to identify small-molecule inhibitors of SARS-CoV-2 M^{Pro}. *J Biomol Struct Dyn.* 2021; 1–17. <https://doi.org/10.1080/07391102.2021.1993341> PMID: 34676801
51. Somboon T, Mahalapbutr P, Sanachai K, Maitarad P, Lee VS, Hannongbua S, et al. Computational study on peptidomimetic inhibitors against SARS-CoV-2 main protease. *J Mol Liq.* 2021; 322: 114999. <https://doi.org/10.1016/j.molliq.2020.114999> PMID: 33518853
52. Sharma P, Joshi T, Mathpal S, Joshi T, Pundir H, Chandra S, et al. Identification of natural inhibitors against Mpro of SARS-CoV-2 by molecular docking, molecular dynamics simulation, and MM/PBSA methods. *J Biomol Struct Dyn.* 2022; 40: 2757–2768. <https://doi.org/10.1080/07391102.2020.1842806> PMID: 33143552
53. J A, Francis D, C.S. S, K.G. A, C. S, Variyar EJ. Repurposing simeprevir, calpain inhibitor IV and a cathepsin F inhibitor against SARS-CoV-2 and insights into their interactions with M^{Pro}. *J Biomol Struct Dyn.* 2022; 40: 325–336. <https://doi.org/10.1080/07391102.2020.1813200> PMID: 32873185
54. Elseginy SA, Anwar MM. *In silico* analysis of SARS-CoV-2 papain-like protease potential inhibitors. *RSC Adv.* 2021; 11: 38616–38631. <https://doi.org/10.1039/D1RA07845C> PMID: 35493238
55. Abd El-Mordy FM, El-Hamouly MM, Ibrahim MT, El-Rheem GA, Aly OM, Abd El-kader AM, et al. Inhibition of SARS-CoV-2 main protease by phenolic compounds from *Manilkara hexandra* (Roxb.) Dubard assisted by metabolite profiling and *in silico* virtual screening. *RSC Adv.* 2020; 10: 32148–32155. <https://doi.org/10.1039/D0RA05679K> PMID: 35518160
56. Allam AE, Assaf HK, Hassan HA, Shimizu K, Elshaier YAMM. An *in silico* perception for newly isolated flavonoids from peach fruit as privileged avenue for a countermeasure outbreak of COVID-19. *RSC Adv.* 2020; 10: 29983–29998. <https://doi.org/10.1039/D0RA05265E> PMID: 35518212
57. Cherrak SA, Merzouk H, Mokhtari-Soulimane N. Potential bioactive glycosylated flavonoids as SARS-CoV-2 main protease inhibitors: A molecular docking and simulation studies. Salahub D, editor. *PLOS ONE.* 2020; 15: e0240653. <https://doi.org/10.1371/journal.pone.0240653> PMID: 33057452
58. Swargiary A, Mahmud S, Saleh MdA. Screening of phytochemicals as potent inhibitor of 3-chymotrypsin and papain-like proteases of SARS-CoV2: an *in silico* approach to combat COVID-19. *J Biomol Struct Dyn.* 2022; 40: 2067–2081. <https://doi.org/10.1080/07391102.2020.1835729> PMID: 33089730
59. Arora S, Lohiya G, Moharir K, Shah S, Yende S. Identification of Potential Flavonoid Inhibitors of the SARS-CoV-2 Main Protease 6YNQ: A Molecular Docking Study. *Digit Chin Med.* 2020; 3: 239–248. <https://doi.org/10.1016/j.dcm.2020.12.003>
60. Batool F, Mughal EU, Zia K, Sadiq A, Naeem N, Javid A, et al. Synthetic flavonoids as potential antiviral agents against SARS-CoV-2 main protease. *J Biomol Struct Dyn.* 2022; 40: 3777–3788. <https://doi.org/10.1080/07391102.2020.1850359> PMID: 33251983
61. Xu Z, Yang L, Zhang X, Zhang Q, Yang Z, Liu Y, et al. Discovery of Potential Flavonoid Inhibitors Against COVID-19 3CL Proteinase Based on Virtual Screening Strategy. *Front Mol Biosci.* 2020; 7: 556481. <https://doi.org/10.3389/fmolb.2020.556481> PMID: 33134310
62. Murtuja S, Shilkar D, Sarkar B, Sinha BN, Jayaprakash V. A short survey of dengue protease inhibitor development in the past 6 years (2015–2020) with an emphasis on similarities between DENV and SARS-CoV-2 proteases. *Bioorg Med Chem.* 2021; 49: 116415. <https://doi.org/10.1016/j.bmc.2021.116415> PMID: 34601454
63. Berman HM, Westbrook J, Feng Z, Gilliland G, Bhat TN, Weissig H, et al. The Protein Data Bank. *Nucleic Acids Res.* 2000; 28: 235–242. <https://doi.org/10.1093/nar/28.1.235> PMID: 10592235

64. Dwivedi VD, Arya A, Yadav P, Kumar R, Kumar V, Raghava GP. DenvInD: dengue virus inhibitors database for clinical and molecular research. *Brief Bioinform.* 2021; 22: bbaa098. <https://doi.org/10.1093/bib/bbaa098> PMID: 32510549
65. Schrödinger Release 2020–4: LigPrep, Schrödinger, LLC, New York, NY, 2020.
66. Madhavi Sastry G, Adzhigirey M, Day T, Annabhimoju R, Sherman W. Protein and ligand preparation: parameters, protocols, and influence on virtual screening enrichments. *J Comput Aided Mol Des.* 2013; 27: 221–234. <https://doi.org/10.1007/s10822-013-9644-8> PMID: 23579614
67. Schrödinger Release 2020–4: Glide, Schrödinger, LLC, New York, NY, 2020.
68. Friesner RA, Murphy RB, Repasky MP, Frye LL, Greenwood JR, Halgren TA, et al. Extra Precision Glide: Docking and Scoring Incorporating a Model of Hydrophobic Enclosure for Protein–Ligand Complexes. *J Med Chem.* 2006; 49: 6177–6196. <https://doi.org/10.1021/jm051256o> PMID: 17034125
69. Friesner RA, Banks JL, Murphy RB, Halgren TA, Klicic JJ, Mainz DT, et al. Glide: a new approach for rapid, accurate docking and scoring. 1. Method and assessment of docking accuracy. *J Med Chem.* 2004; 47: 1739–1749. <https://doi.org/10.1021/jm0306430> PMID: 15027865
70. Halgren TA, Murphy RB, Friesner RA, Beard HS, Frye LL, Pollard WT, et al. Glide: a new approach for rapid, accurate docking and scoring. 2. Enrichment factors in database screening. *J Med Chem.* 2004; 47: 1750–1759. <https://doi.org/10.1021/jm030644s> PMID: 15027866
71. Schrödinger Release 2020–4: Maestro, Schrödinger, LLC, New York, NY, 2020.
72. Bowers KJ, Chow DE, Xu H, Dror RO, Eastwood MP, Gregersen BA, et al. Scalable Algorithms for Molecular Dynamics Simulations on Commodity Clusters. *ACM/IEEE SC 2006 Conference (SC'06).* Tampa, FL: IEEE; 2006. pp. 43–43.
73. Schrödinger Release 2020–4: Desmond Molecular Dynamics System, D.E. Shaw Research: New York, NY, 2020; Maestro-Desmond Interoperability Tools; Schrödinger: New York, NY, USA. 2020.
74. Schrödinger Release 2020–4: Prime, Schrödinger, LLC, New York, NY, 2020.
75. Jacobson MP, Pincus DL, Rapp CS, Day TJ, Honig B, Shaw DE, et al. A hierarchical approach to all-atom protein loop prediction. *Proteins Struct Funct Bioinforma.* 2004; 55: 351–367. <https://doi.org/10.1002/prot.10613> PMID: 15048827
76. Jacobson MP, Friesner RA, Xiang Z, Honig B. On the role of the crystal environment in determining protein side-chain conformations. *J Mol Biol.* 2002; 320: 597–608. [https://doi.org/10.1016/s0022-2836\(02\)00470-9](https://doi.org/10.1016/s0022-2836(02)00470-9) PMID: 12096912
77. Li J, Abel R, Zhu K, Cao Y, Zhao S, Friesner RA. The VSGB 2.0 model: a next generation energy model for high resolution protein structure modeling. *Proteins.* 2011; 79: 2794–2812. <https://doi.org/10.1002/prot.23106> PMID: 21905107
78. Pathania S, Singh PK. Analyzing FDA-approved drugs for compliance of pharmacokinetic principles: should there be a critical screening parameter in drug designing protocols? *Expert Opin Drug Metab Toxicol.* 2021; 17: 351–354. <https://doi.org/10.1080/17425255.2021.1865309> PMID: 33320017
79. Ainsley J, Chaturvedi SS, Karabencheva-Christova TG, Tanasova M, Christov CZ. Integrating molecular probes and molecular dynamics to reveal binding modes of GLUT5 activatory and inhibitory ligands. *Chem Commun.* 2018; 54: 9917–9920. <https://doi.org/10.1039/c8cc04843f> PMID: 30113044
80. Kaushik AC, Kumar A, Rehman AU, Junaid M, Khan A, Bharadwaj S, et al. Deciphering G-protein-coupled receptor 119 agonists as promising strategy against type 2 diabetes using systems biology approach. *Acs Omega.* 2018; 3: 18214–18226.
81. Thiel V, Ivanov KA, Putics Á, Hertzig T, Schelle B, Bayer S, et al. Mechanisms and enzymes involved in SARS coronavirus genome expression. *J Gen Virol.* 2003; 84: 2305–2315. <https://doi.org/10.1099/vir.0.19424-0> PMID: 12917450
82. Shu T, Huang M, Wu D, Ren Y, Zhang X, Han Y, et al. SARS-CoV-2 Nsp13 Possesses NTPase and RNA Helicase Activities That Can Be Inhibited by Bismuth Salts. *Virol Sin.* 2020; 35: 321–329. <https://doi.org/10.1007/s12250-020-00242-1> PMID: 32500504
83. Keillor JW, Brown RS. Attack of zwitterionic ammonium thiolates on a distorted anilide as a model for the acylation of papain by amides. A simple demonstration of a bell-shaped pH/rate profile. *J Am Chem Soc.* 1992; 114: 7983–7989. <https://doi.org/10.1021/ja00047a004>
84. Ullrich S, Nitsche C. The SARS-CoV-2 main protease as drug target. *Bioorg Med Chem Lett.* 2020; 30: 127377. <https://doi.org/10.1016/j.bmcl.2020.127377> PMID: 32738988
85. Mengist HM, Dilnessa T, Jin T. Structural basis of potential inhibitors targeting SARS-CoV-2 main protease. *Front Chem.* 2021; 9: 622898. <https://doi.org/10.3389/fchem.2021.622898> PMID: 33889562
86. Bafna K, Krug RM, Montelione G. Structural Similarity of SARS-CoV2 Mpro and HCV NS3/4A Proteases Suggests New Approaches for Identifying Existing Drugs Useful as COVID-19 Therapeutics. *Chemistry.* 2020 Apr. <https://doi.org/10.26434/chemrxiv.12153615> PMID: 32511291

87. Gentile D, Patamia V, Scala A, Sciortino MT, Piperno A, Rescifina A. Putative Inhibitors of SARS-CoV-2 Main Protease from A Library of Marine Natural Products: A Virtual Screening and Molecular Modeling Study. *Mar Drugs*. 2020; 18: 225. <https://doi.org/10.3390/MD18040225> PMID: 32340389
88. Su H, Yao S, Zhao W, Li M, Liu J, Shang W, et al. Discovery of baicalin and baicalein as novel, natural product inhibitors of SARS-CoV-2 3CL protease *in vitro*. *Molecular Biology*; 2020 Apr. <https://doi.org/10.1101/2020.04.13.038687>
89. Al-Karmalawy AA, Dahab MA, Metwaly AM, Elhady SS, Elkaeed EB, Eissa IH, et al. Molecular Docking and Dynamics Simulation Revealed the Potential Inhibitory Activity of ACEIs Against SARS-CoV-2 Targeting the h ACE2 Receptor. *Front Chem*. 2021; 9: 661230. <https://doi.org/10.3389/fchem.2021.661230> PMID: 34017819
90. Bharadwaj S, Dubey A, Yadava U, Mishra SK, Kang SG, Dwivedi VD. Exploration of natural compounds with anti-SARS-CoV-2 activity via inhibition of SARS-CoV-2 Mpro. *Brief Bioinform*. 2021; 22: 1361–1377. <https://doi.org/10.1093/bib/bbaa382> PMID: 33406222
91. Kumar S, El-Kafrawy SA, Bharadwaj S, Maitra S, Alandijany TA, Faizo AA, et al. Discovery of bispecific lead compounds from Azadirachta indica against ZIKA NS2B-NS3 Protease and NS5 RNA dependent RNA polymerase using molecular simulations. *Molecules*. 2022; 27: 2562. <https://doi.org/10.3390/molecules27082562> PMID: 35458761